Global ocean heat content redistribution during the 1998–2012 Interdecadal Pacific Oscillation negative phase

Guillaume Gastineau, Andrew R. Friedman, Myriam Khodri, Jérôme Vialard

Global ocean heat content redistribution during the 1998-2012 Interdecadal Pacific Oscillation negative phase

Guillaume Gastineau[1], Andrew R. Friedman[1,2], Myriam Khodri[1], and Jérôme Vialard[1]

[1] *Sorbonne-Université, LOCEAN, CNRS/IRD/UPMC/MNHN, Paris, France*

[2] *Now at School of Geosciences, University of Edinburgh, UK*

June 8th 2018,

Submitted to Climate Dynamics

Corresponding author address: Dr Guillaume Gastineau, Sorbonne Université, UPMC/CNRS/IRD/MNHN, LOCEAN/IPSL, 4 place Jussieu, 75005 Paris, France.

E-mail: guillaume.gastineau@upmc.fr

Abstract

Previous studies have linked the slowdown in global surface temperature warming since 2000 to a negative Interdecadal Pacific Oscillation (IPO) phase. Here, we investigate the changes in ocean heat content (OHC) during this period. We compare two ensembles of coupled model experiments with either zero or observed prescribed tropical Pacific wind stress interannual anomalies. This successfully constrains the global surface temperature, sea level pressure and OHC patterns associated with the IPO phase transition around 1998. The negative IPO phase (1998 to 2012) is associated with a global ocean heat redistribution. The anomalously cold tropical Pacific Ocean leads to an increased oceanic uptake in this region, and a global OHC increase of $4x10^{22}$ J. The cold equatorial Pacific also forces mid-latitude wind changes through atmospheric teleconnections, leading to an enhanced wind-driven heat transport convergence at 40°N and 40°S. Enhanced Pacific easterlies also yield an enhanced heat transport to the Indian Ocean via the Indonesian throughflow. As a result, the anomalous Pacific heat uptake is entirely exported towards the North Pacific (~50%), Indian (~30%) and Southern (~20%) Oceans. A significant fraction of this heat is released back to the atmosphere in the North Pacific and Indian basins, and transported across 31°S in the Indian Ocean. Overall, OHC increases most in the Southern Ocean (~60% of global changes) and northern Pacific (~40%), with negligible changes in the Indian and Atlantic basins. These results point to the major importance of oceanic circulation in re-distributing the Pacific heat uptake globally during negative IPO phases.

Keywords: Decadal climate variability, Pacific Ocean, global warming, ocean heat content, air-sea interactions

1. Introduction

The continued increase in atmospheric greenhouse gas (GHG) concentrations since the Industrial Revolution induces a positive imbalance in the top-of-atmosphere (TOA) planetary energy budget (e.g. Hansen et al., 2005; Trenberth et al., 2009). The overwhelming majority of this excess energy is absorbed by the oceans, as they have a dominant heat capacity (Bindoff et al., 2013; Trenberth et al., 2014). Some of this heat also warms the atmosphere, leading to a steady rise in global mean surface temperature. In the 15-year period from around 1998 to 2012, however, the global mean surface temperature displayed a relatively weak warming rate compared to the previous decades (Easterling et al., 2009). This reduction in the rate of surface warming has been called the *hiatus* or *slowdown* in the global surface warming (Yan et al., 2016; Medhaug et al., 2017). Several recent studies largely attribute this change in the warming rate to natural climate variability, and more specifically to a prolonged abnormally cold sea surface temperature (SST) in the tropical Pacific Ocean (Meehl et al., 2011; Kosaka and Xie, 2013; Fyfe and Gillett, 2014; Clement and DiNezio, 2014; Trenberth, 2015; Dai et al., 2015).

The tropical Pacific Ocean is home to the El Niño Southern Oscillation (ENSO; e.g. McPhaden et al., 2006), the dominant climate mode on earth at interannual timescales (e.g. Deser et al., 2010). The ENSO negative phase, La Niña, is associated with a cold central and eastern Pacific, reduced convection in the central Pacific, and abnormally strong easterlies. The changes in tropical convection and associated convective heating during ENSO events induce remote changes in sea level pressure (SLP), surface winds and SST through atmospheric teleconnections, i.e. planetary waves towards the mid-latitudes channelled along mean-state dependent waveguides (e.g. Horel and Wallace 1981; Trenberth et al., 1998). This creates in particular the horseshoe-shaped cold SST anomaly pattern associated with warm anomalies in the northwestern and southwestern Pacific sectors during La Niña events. The

low-frequency tail of ENSO variations is associated with decadal-scale SST anomalies in the tropical Pacific, and the associated global SST pattern is called the Interdecadal Pacific Oscillation (IPO; Zhang et al., 1997; Power et al., 1999).

The IPO shifted from a warm to a cold phase around 1998, yielding a cooling trend of central and eastern Pacific SST, associated with an unprecedented intensification of the Pacific Walker circulation (Kociuba and Power, 2015; Choi et al., 2016) and strengthening of Pacific trade winds during the 20-year period beginning around 1992 (Balmaseda et al., 2013; England et al., 2014; de Boisséson et al., 2014). Several studies identified this negative IPO phase during the 1998-2012 period as an important driver of the hiatus, due to the associated internal rearrangement of heat within the climate system. A positive imbalance of ~0.5–1 W m^2 in the TOA planetary energy budget was indeed observed during this period (Loeb et al., 2012; Allan et al., 2014, Johnson et al., 2016), although volcanic activity and anthropogenic aerosols may have contributed to a small reduction in absorbed solar radiation (Solomon et al., 2011; Santer et al., 2014; Ridley et al., 2014; Smith et al., 2015). This observed imbalance implies that the total heat in the climate system steadily increased during the hiatus, and a smaller fraction of this heat was used to warm the atmosphere. Several studies suggested that the abnormally cold Pacific favored an enhanced oceanic heat uptake during this period (Meehl et al., 2011; Kosaka and Xie, 2013, Douville et al., 2015; England et al., 2014, Watanabe et al., 2014), with increased downward heat flux into the ocean in the tropical Pacific, yielding a larger global OHC increase in the subsurface during the negative IPO phase. Drijfhout et al. (2014) found that the ocean heat uptake was also modified in other basins, such as the Southern and subtropical Indian Oceans or the subpolar North Atlantic. Some of these studies used *pacemaker* experiments specifying observed anomalies of either SST (Kosaka and Xie, 2013; Douville et al., 2015) or wind (England et al., 2014; Watanabe et al., 2014; Douville et al., 2015) over the tropical or central/eastern Pacific. This

setup results in more realistic global SST patterns due to the remote impacts of Pacific SST anomalies through teleconnections, and a reduced rate of global surface temperature warming over the last two decades (e.g. Kosaka and Xie, 2013).

A burning question is thus: where did the extra heat pumped into the Pacific during the hiatus decade go? This question is not easy to tackle from observations alone. Deep ocean observations are indeed too sparse to track the OHC changes, even with improved recent estimates (Cheng et al., 2017). The deployment of Argo floats in the early 2000s greatly improved the sampling (Lyman, 2012; Abraham et al., 2013), but the current configuration of Argo floats only reliably samples the upper 2000m of the ocean. In addition, observed changes are a combination of the effects of global warming and natural decadal variability, so that it is not easy to isolate the heat redistribution related to negative IPO phases from observations only (Liu et al., 2016a). There is hence so far little consensus on the location of OHC changes associated with the IPO. Meehl et al. (2011) point to the deep ocean, below 750m in Atlantic and the Southern Ocean, and below 300m in the Pacific and the Indian Ocean. England et al. (2014) suggest an increased OHC in the upper 350m of the tropical Pacific. Some studies suggest that a large fraction of the Pacific heat uptake has been transferred to the Indian Ocean via the Indonesian Throughflow (Lee et al., 2015; Nieves et al., 2015; Liu et al., 2016a). However, other studies combining model and observations have pointed out that the La Niña-related Pacific and Indian OHC increases in upper layers are not enough to account for the early 21st century warming slowdown, and that OHC increases at deeper layers in the Atlantic and Southern Ocean account for most of the sequestration (Chen and Tung, 2014; Drijfhout et al., 2014; Roemmich et al., 2015; Llovel and Terray, 2016; Oka and Watanabe, 2017). Cheng et al. (2017) also verified that such a warming in the Atlantic and Southern Ocean has occurred in observations. Liu et al. (2016a, 2016b) have however argued that the deep Atlantic and Southern Ocean observed warming are due to

anthropogenic climate change, and not specifically to a negative IPO phase, a point which is contested by Chen and Tung (2016). The relative contributions of various ocean basins to OHC changes during the recent negative IPO phase and the associated processes thus remain controversial.

This study aims at quantifying the OHC changes in each basin during the early 21st century hiatus period, and the associated processes, partitioning the relative contributions from surface heat uptake and lateral redistribution by the oceanic circulation. We use a coupled model with a *pacemaker* setup in the tropical Pacific to constrain the global IPO pattern through atmospheric teleconnections, as in previous studies. We will show that the resulting coupled model global surface temperature, SLP and OHC variations match those related to the IPO in observations. The global anomalous response associated with the IPO is obtained as the difference with a twin simulation with identical radiative forcings in which the *climatological* tropical Pacific wind stress is imposed. We then use a heat budget approach to examine the global OHC changes and their causes.

The paper is structured as follows: section 2 discusses the modelling setup and methodology; section 3 describes the global signals remotely driven by the strengthened easterlies and the resulting cold anomaly in the tropical Pacific; section 4 evaluates the associated ocean heat content changes, and analyses the related surface heat uptake and oceanic heat transport. We summarize and discuss the implications of our results in Section 5.

2. Methods and Data

144 *2.1 Coupled model*

145 We use the coupled IPSL-CM5A-LR global climate model (Dufresne et al., 2013).
146 The atmospheric component is LMDZ5A (Hourdin et al., 2013), with a resolution of 3.75° ×
147 1.875° with 39 vertical levels. The land surface component is ORCHIDEE (Krinner et al.,
148 2005), with the same resolution as the atmosphere. The ocean component is NEMOv3.2
149 (Madec, 2008) coupled to the LIM2 sea ice model (Fichefet and Maqueda, 1997). It uses a
150 resolution of about 2°, with a refinement to 0.5° meridional resolution near the equator, and
151 31 vertical levels.

152 IPSL-CM5A-LR simulates the El Niño–Southern Oscillation (ENSO) amplitude,
153 structure, and spectrum reasonably (Bellenger et al., 2014), although it displays an incorrect
154 seasonal phase locking. It simulates well the main characteristics of the North Pacific
155 variability (Fleming and Anchukaitis, 2016), the links between ENSO and IPO (Nidheesh et
156 al., 2017), the tropical intra-seasonal variability (Maury et al., 2013; Hung et al., 2013) and
157 the North Atlantic variability (Cattiaux et al., 2013; Gastineau et al., 2013). However, like
158 many global climate models, IPSL-CM5A-LR has a double intertropical convergence zone
159 (ITCZ) bias and a too strong equatorial upwelling in the Pacific (Dufresne et al. 2013).
160 Compared to other Coupled Model Intercomparison Project Phase 5 (CMIP5; Taylor et al.,
161 2012) climate models, IPSL-CM5A-LR also has relatively large transient and equilibrium
162 climate sensitivities to CO_2 doubling (Forster et al., 2013). This response is mainly due to a
163 large positive low-cloud feedback (Brient and Bony, 2013; Andrews et al., 2012).
164

165 *2.2 Experimental protocol*

166 We perform two ensembles of partially-coupled simulations using IPSL-CM5A-LR
167 from 1979 to 2014. In the two ensembles, we use the standard CMIP5 GHG, aerosol and
168 ozone forcings (Taylor et al., 2012), following the historical experiments through 2005 and

RCP8.5 from 2006 to 2014. Volcanic stratospheric aerosol forcings are applied by prescribing the aerosol optical depth, as given in Sato et al. (1993; 2012 updated version). 30 members are run for each of the two ensembles. Each ensemble was initialised in 1979 from a 30-member ensemble of fully-coupled historical simulations starting in 1940, described in more detail in Frankignoul et al. (2017).

We perform two ensembles, with a pacemaker approach designed to constrain the Pacific interannual variability. The first ensemble, W-CLIM, is meant as a reference representative of a neutral IPO phase. The second ensemble, W-FULL, is constrained to follow the observed IPO evolution. In these simulations, the wind stress is prescribed in the ocean model in the tropical Pacific, while coupling operates normally over the rest of the world. The surface wind stress is prescribed within the tropical Pacific from 20°S to 20°N, from the Indonesian archipelago to the west coast of Central and South America, with a buffer zone between 15° and 25° latitude to avoid discontinuities, as shown by the black contours in Fig. 1a. The surface turbulent heat fluxes are unchanged in the model, so that the sensible and evaporative fluxes are calculated using the interactive model wind. We prefer this approach to nudging SST anomalies because it yields a conservative ocean-atmosphere heat exchange (Douville et al., 2015).

The coupled model long-term wind stress climatology is applied in the tropical Pacific in W-CLIM. This long-term climatology is estimated as the 1979–2014 average of 6 members from the IPSL-CM5A-LR historical CMIP5 ensemble (1979 to 2005) and 4 members from RCP8.5 CMIP5 ensemble (2006 to 2014), smoothed (Lanczos filter, 30-day cutoff period) to remove noise. As the mixed layer dynamics is parameterized using a turbulent kinetic energy closure scheme (Madec, 2008), the high frequency variability of the wind stress linked to weather noise is important to estimate correctly the mixing within the oceanic mixed layer, as mentioned in Lee et al. (2015). High frequency winds indeed induce

194 a vertical shear, which in turn generates turbulence and deepens the mixed layer. Therefore,
195 we add randomly scrambled high-frequency (3–30 day band-passed) wind stress anomalies
196 from the ERA-Interim reanalysis (Dee et al., 2011) to the model climatological values.
197 Figure 1b shows the zonal wind stress model climatology averaged over the Niño 4 region
198 (160°E–150W°, 6°S–6°N). Though the trade winds are weaker in the model, the seasonal
199 cycle agrees with ERA-Interim, with maximum values in January, and minima in boreal
200 spring and fall.
201 The second experiment, referred to as W-FULL, uses the daily wind stress anomalies
202 from ERA-Interim from 1979–2014 added to the IPSL-CM5A-LR model climatology. The
203 daily wind stress anomalies were obtained by subtracting the daily ERA-Interim 1979–2014
204 climatology.
205
206 *2.3 Ocean heat content and heat transport*
207 OHC is calculated from:
208 $$OHC = \int \rho_0 C_p \, T \, dz \qquad (1)$$
209 where C_P is the seawater specific heat capacity. T is the potential temperature field and ρ_0 is
210 the seawater density (i.e. 1025 kg m^{-3}). z denotes depth. We decompose the OHC variations
211 using a simple heat budget:
212 $$\Delta OHC = \bar{F}\Delta t + \left(\int \rho_0 C_p \, \boldsymbol{\nabla} \left(\overline{\boldsymbol{u}.T}\right) dz\right) \Delta t \; + \; R \qquad (2)$$
213 where $\boldsymbol{u}$ is the current, and F, the local surface heat flux anomaly at the ocean surface,
214 positive downward. Δt denotes the length of the time period considered. ΔOHC is the OHC
215 variation over the time period. The overline designates monthly average. The first term on the
216 right hand side is the surface heat uptake, which includes the effect of air/sea heat exchanges.
217 This term is calculated from the heat fluxes on the oceanic grid. The second term is the ocean
218 heat transport divergence and represents the influence of the ocean circulation. This term is

219 calculated from the monthly vertically-integrated ocean heat transport calculated on-line by
220 the ocean model, including the eddy-induced (bolus) velocity calculated by the Gent and
221 McWilliams (1990) parameterization, but without accounting for the ocean transport due to
222 diffusive lateral mixing (outputs not available). The last term, *R*, is calculated as a residual
223 and accounts for the contributions from diffusive lateral mixing and changing sea ice heat
224 content. We will show in Section 4.3 that this term is small for the time period we consider.

225 OHC is an extensive variable and is sensitive to the area of the oceanic grid cell. To
226 avoid any influence of the grid cell area, the maps shown in the following illustrate the OHC
227 per unit area (J m^{-2}), while the OHC integrated over the different basins is in J.

228

229 *2.4 Observations and reanalysis data*

230 We use the SLP and 2m surface air temperature data from the ERA-Interim reanalysis
231 (Dee et al., 2011) from the European Center for Medium-Range Weather Forecasts
232 (ECMWF). For SST, we mainly use the monthly NOAA Optimal Interpolation SST
233 Analysis, version 2 (OISST) (Reynolds et al., 2002); we also examine HadISST1 (Rayner et
234 al., 2003) after removal of the global warming signal using an optimal filter based on linear
235 inverse modeling from Frankignoul et al. (2017). We take monthly sea surface height (SSH)
236 from the Archiving, Validation and Interpretation of Satellite Oceanographic (AVISO)
237 dataset (Nerem et al., 2010), gridded ocean fields from the Ocean Reanalysis System 4
238 (ORAS4; Balmaseda et al. 2013), and surface heat fluxes from the TropFlux product (Kumar
239 et al. 2012).

240

241 *2.5 Climate indices*

242 We use the Niño 3.4 index as a standard metric for ENSO: the SST anomaly over
243 120°–170°W and 6°S–6°N. The east–west thermocline tilt is given by the average 6°S–6°N

20°C isotherm depth in 120°E–170°W minus that in 150°–80°W. In order to analyse the IPO, we use the SST tripole index (TPI, Henley et al. 2015), defined as the central equatorial Pacific SST (170°E–90°W, 10°S–10°N) minus the average of northwest (140°E–145°W, 25°–45°N) and southwest (150°E–160°W, 15°–50°S) Pacific SST, smoothed using a 1-3-4-3-1 filter (Trenberth et al., 2007). The equatorial Pacific zonal SLP gradient, defined as the area-averaged SLP in the eastern (160°–80°W, 6°S–6°N) minus that in the western equatorial Pacific (80°–160°E, 6°S–6°N**)** is used as a proxy of the Walker circulation (Vecchi et al. 2006; Kociuba and Power 2015). To evaluate the atmospheric circulation changes in the mid-latitudes we also use the averaged SLP over the North Pacific (as in the North Pacific Index, Trenberth and Hurrell 1994) and the Amundsen Sea, defined over 160°E–140°W, 30°–65°N and 170°E–70°W, 60°–75°S respectively. Lastly, we use the normalized difference between 35°N and 65°N of the zonally averaged sea-level pressure (SLP) in 80°W-30°E as a NAO index (Li et al., 2013).

2.6 Trend analysis and statistical testing

In time series plots, the ensemble mean is displayed, and the ensemble spread is depicted using 95% confidence intervals for the ensemble mean. We will first focus on the 21-year period of strengthening Pacific trade winds (Balmaseda et al., 2013; de Boisséson et al., 2014; England et al., 2014) to investigate if W-FULL successfully describes the associated transition from a positive to negative IPO global pattern. Unless stated otherwise, trends are reported for annual means. The level of statistical significance of simulated trends is evaluated using two-tailed Student *t*-tests, using the values of all members. Correlations between observations and simulations are based on linearly detrended values, and use the ensemble means. The significance level of observed trends and correlations between observations and simulations is calculated using a *t*-test, adjusting the standard error and the

degrees of freedom following a first order autoregressive process (Bretherton et al., 1999; Santer et al., 2000). As the TPI is smoothed using a low-pass filter, we estimate the level of significance of the TPI trend using the adjusted standard error from an ARMA(1,1) model (Foster and Rahmstorf, 2011). Trend and correlation values are given in boldface if they are statistically significant at the 95% confidence level.

3. Climatic impacts of the increasing tropical Pacific wind stress

3.1 Pacific sea surface temperature

The observed wind stress anomaly in the Niño 4 region (Fig. 1c) displays a strengthening trend of **$-1.65\ 10^{-2}$** Pa decade^{-1} over 1992–2012 consistent with previous studies (Balmaseda et al., 2013; de Boisséson et al., 2014; England et al., 2014). It also displays clear ENSO-related interannual variability, to which the east-west tilt in the thermocline (Fig. 1d, **0.98** correlation with ORAS4 reanalysis) and SST anomalies in the central Pacific (Fig. 1e, **0.91** correlation with OISST) respond. W-FULL is able to reproduce observed ENSO SST and thermocline variations in response to the prescribed observed wind stress anomalies. This is consistent with the well-known dominant role of wind anomalies for the thermocline depth at the equator and for the ocean temperature (Sarachik and Cane, 2010), while the different amplitudes might be due to the heat flux feedback, which depends on the coupled model used (Bellenger et al., 2014). At longer timescales, W-FULL reproduces the increasing east-west thermocline tilt and cooling SST trend in the central Pacific associated with strengthening easterlies (see Table 1). Overall, W-FULL reproduces the observed tropical Pacific decadal variability, capturing the transition from the more predominant El-Niños in the 1990s to the more predominant La Niñas in the 2000s.

293 Conversely, imposing the wind stress climatology in W-CLIM (Figs. 1d and 1e, red
294 line) yields no interannual variability in thermocline tilt. As a result there is no interannual
295 variability in SST, except for the cooling following the Pinatubo (1991) and El Chichón
296 (1982) volcanic eruptions. W-CLIM also reveals a warming trend associated with the
297 imposed evolution of GHG (Table 1), that is difficult to see in W-FULL due to the larger
298 interannual and decadal variations.
299 W-FULL hence reproduces Pacific ENSO variations and their decadal modulation,
300 including the transition from a warm phase in the 1990s to a cold phase in the 2000s. W-
301 FULL also reproduces the IPO time evolution (Fig. 1f), with the observed transition from the
302 positive to negative IPO around 1998, again with an overestimated amplitude. In the
303 following sections, we will investigate the associated atmospheric changes.
304
305 *3.2 Surface air temperature*
306 W-CLIM (Fig. 2a) features a broad-scale positive 1992–2012 2m air temperature
307 trend, with larger amplitudes over land and reduced warming in the Southern Ocean and
308 subpolar North Atlantic, consistent with the global warming pattern simulated by most
309 models (e.g. Stouffer et al., 1989). In contrast, W-FULL (Fig. 2b) features a prominent
310 cooling across the tropical Pacific, and enhanced warming near the Kuroshio extension and
311 around 40°S, consistent with the trend toward a negative IPO. Comparison with the ERA-
312 Interim 2m temperature trend (Fig. 2c) indicates that W-FULL largely captures the observed
313 negative IPO-like trend pattern, with an overestimated amplitude and an equatorial cooling
314 that extends too far westward, consistent with the cold tongue bias in that model (Bellenger
315 et al. 2014).
316 Figure 2d displays annual global mean 2m air temperature time series, with the 1992–
317 2012 trend values in Table 1. The 1992–2012 ensemble mean trend is significantly smaller in

W-FULL than W-CLIM, and much closer to ERA-Interim. Imposing observed wind stress anomalies in the Pacific leads to a more realistic rate of global warming, as in previous similar experiments (England et al. 2014; Watanabe et al. 2014; Douville et al., 2015; Thoma et al. 2015). The W-FULL surface temperature trend is still greater than observations, reflecting the large IPSL-CM5A-LR climate sensitivity (Forster et al. 2013). Overall, the tropical Pacific changes yield a global temperature response that is broadly consistent with the observed changes from 1992 to 2012. Next, we explore the corresponding atmospheric circulation changes.

3.3 Large-scale atmospheric circulation changes

Figure 3 shows the 1992–2012 SLP trend to illustrate the large-scale atmospheric circulation changes during that period. W-CLIM SLP trends (Fig. 3a) are weak, with lower SLP in the tropics as the SST warms and an increase of SLP at 40° over the northern and southern mid-latitudes as the Hadley circulation expands poleward under climate change (Lu et al. 2008). There is also a SLP decrease over the Arctic induced by the large surface warming in that region (see Fig. 2a). W-FULL (Fig. 3b) displays much larger SLP trends than W-CLIM, with a SLP increase in the eastern tropical Pacific and decrease in the western Pacific and Indian Oceans, consistent with an enhanced Walker circulation. These changes are broadly consistent with ERA-Interim (Fig. 3c), though the W-FULL positive SLP anomaly in the eastern equatorial is overestimated and extends too far westward. The equatorial Pacific zonal SLP gradient, ΔSLP (Fig. 3d), illustrates that the Walker circulation in W-FULL (Fig. 3d) reproduces the observed variations of the Pacific easterlies (correlation of **0.81**) and its 1992–2012 strengthening trend, albeit with larger amplitude. Therefore, constraining the wind stress yields realistic SST variations in the equatorial Pacific (Fig. 1e) that in turn constrain the equatorial Pacific Walker circulation.

343 The W-FULL extratropical Pacific SLP changes (Fig. 3b) display large anticyclonic
344 anomalies over the Aleutian Low and the southern Pacific Ocean at 40°S, while cyclonic
345 anomalies are simulated over the Amundsen Sea. Such SLP anomalies are also found in
346 ERA-Interim (Fig. 3c; also see the North Pacific and Amundsen Sea Low indices in Table 1).
347 These SLP changes are consistent with those expected from ENSO teleconnections. El Niños
348 indeed yield a deeper Aleutian Low, negative SLP anomalies at ~30-50°S in the Pacific and
349 south of Australia (e.g. Sterl et al. 2007) and a weaker than usual Amundsen low (e.g. Fogt et
350 al. 2012; Turner et al. 2013; Clem and Renwick, 2015; Meehl et al., 2016), with roughly
351 opposite signals during La Niñas. The transition from a positive (more Niños) to a negative
352 (more Niñas) IPO phase hence yields the signals in Figs. 3b and 3c. It also explains the
353 significant trends that are similar for observations and W-FULL for the averaged SLP over
354 the North Pacific and Amundsen Sea (Table 1).
355 Over the Atlantic, W-FULL does not simulate the observed extratropical SLP changes,
356 as illustrated by the NAO index trend in Table 1. The 1992–2012 W-FULL trend shows a
357 SLP dipole over the North Atlantic centered over the western part of the basin that projects
358 onto a positive NAO pattern, which is consistent with the response to La Niña conditions (see
359 Gastineau et al., 2013; their Fig. 15). The observations however display an opposite trend,
360 with a weak and insignificant trend toward a negative NAO-like pattern. The ensemble mean
361 displayed for the model filters out internal atmospheric variability and reveals more clearly
362 the response from the changing IPO, while the internal variability over the Atlantic Ocean
363 dominates in observations.
364 The above analysis suggests that constraining the ENSO phase in the tropical Pacific
365 reproduces most of the observed large-scale atmospheric circulation trends in the tropical
366 Indo-Pacific and extratropical Pacific. Those changes are consistent with the expected ENSO

teleconnections when going from a positive to a negative IPO phase. In the following section, we examine the OHC changes associated with these large-scale atmospheric changes.

4. Evaluation of the ocean heat content changes

In this section, we will first illustrate the global OHC changes attributable to the IPO over 1979-2014. We will then focus on the 1998-2012 negative IPO phase, and first show that the global SST anomalies and OHC changes during this period are consistent with observed ones. We will then illustrate the geographical distribution of the OHC changes attributable to the 1998-2012 negative IPO phase, and their origin (surface heat uptake or oceanic transport). We will end by detailing the mechanisms responsible for the heat uptake and redistribution by oceanic transport.

4.1 Global energy balance and ocean heat content evolution

We first diagnose and quantify the global OHC changes and their causes. W-FULL and W-CLIM both display a stable TOA radiative imbalances from 1995 onward of about 1.2 W m^{-2} (not shown), when accounting from energy nonconservation in the atmosphere by removing the value from the TAO imbalance calculated over the whole preindustrial control simulation, as in Hobbs et al. (2016). This value is larger that the present-day observed estimate, which ranges between 0.5 and 1 W m^{-2} (Loeb et al. 2012; Allan et al. 2014; Johnson et al., 2016), and reflects the large climate sensitivity of IPSL-CM5A-LR (Brient and Bony 2013; Andrews et al. 2012). The monthly globally-integrated OHC increases throughout 1995-2014 in both W-FULL and W-CLIM due to this TOA imbalance (Fig. 4a).

The globally-averaged difference between the two simulations, which filters out the influence of the common radiative forcing in each simulation, only retains the changes associated with the IPO. Assuming that the climate variations simulated in W-FULL are a

392 linear superposition of the global warming simulated in W-CLIM and the IPO-related
393 changes, taking the difference W-FULL minus W-CLIM should also remove the changes
394 induced by the large climate sensitivity of the model used. The average monthly heat flux
395 into the ocean (positive downward) in Fig. 4b displays sustained positive anomalies after
396 1998, and variations from positive to negative anomalies before 1998. This is related to a
397 larger TOA radiative imbalance of 0.11 (0.02) W m^{-2} in W-FULL during 1998-2012 (1979-
398 1997) linked to the more frequent La Niña after 1998, as found in observations (Allan et al.,
399 2014). As a result, the accumulated heat into the global ocean (orange curve on Fig. 4c)
400 displays a steady rise from 1998 onward. The global OHC variations (black curve on Fig. 4c)
401 closely track those of the integrated heat fluxes, which confirms that the heat budget is closed
402 at the global scale. As 1998-2012 experiences most of the IPO-related OHC increase,
403 hereafter we will focus on this period to track the OHC changes associated with the IPO
404 negative phase. We will discuss the OHC changes occurring before 1998 in section 5.
405
406 *4.2 SST and OHC changes during the period 1998–2012*
407 Since we focus on the 1998-2012 IPO negative phase, we investigate the SST
408 anomalies and OHC changes during this period. The 1998–2012 W-FULL minus W-CLIM
409 SST anomalies (Fig. 5a) illustrate that this period corresponds to a typical negative IPO phase,
410 with a pattern that agrees well with observational SST anomalies after removal of the global
411 warming signal (Fig. 5b, see section 2.4 for details). The model and observations both display
412 an anomalously cold tropical Pacific. The trademark horseshoe pattern associated with La
413 Niña, with warm SST anomalies in the Kuroshio extension region and subtropical Southern
414 Pacific, broadly agree in the model and observations. The too strong and westward cold
415 anomalies in the tropical Pacific reflect the typical cold tongue bias of the model.

The OHC changes between early 1998 and late 2012 (hereafter, ΔOHC) in W-CLIM (Fig. 6a) display a relatively uniform increase, with heat content mostly increasing in the top 300m (not shown). OHC actually diminishes between 10°N and 20°N in the Pacific, presumably in response to a northward shift of the ITCZ. It also decreases in the eastern North Atlantic as the Atlantic Meridional Overturning circulation (AMOC) slows down (Drijfhout et al., 2012). ΔOHC in W-CLIM however bears little resemblance to the ORAS4 estimate (Fig. 6c). On the other hand, the W-FULL ΔOHC (Fig. 6b) displays a much better agreement with observations (Fig. 6c). In particular, OHC diminishes over the eastern tropical Pacific and increases over the western tropical Pacific, consistent with the anomalously strong easterlies during that period (e.g. England et al. 2014). While this is expected due to the prescribed wind stress anomalies in the tropical Pacific in W-FULL, W-FULL also better reproduces OHC changes in other regions. For instance, both W-FULL and ORAS4 display increasing OHC over the Kuroshio extension, the southwestern Pacific, and (to a lesser extent) the eastern tropical Indian Ocean and Gulf Stream extension regions. The better agreement of W-FULL than W-CLIM with the observed 1998-2012 OHC changes shows that our methodology constrains reasonably the OHC changes associated with the IPO, at least over the Indo-Pacific.

Hereafter, the 1998-2012 W-FULL minus W-CLIM OHC changes, i.e. the changes attributable to the negative IPO phase, are called $\Delta \mathrm{OHC}_{-\mathrm{IPO}}$. The negative IPO is associated with an OHC increase in the western tropical Pacific, and around 40° latitude in both hemispheres (Fig. 7a). On the other hand, there is a clear OHC decrease in the eastern tropical Pacific and at 60°S in the Pacific sector. The vertical distribution of $\Delta \mathrm{OHC}_{-\mathrm{IPO}}$ reveals that the most pronounced OHC changes are located in the upper 300m in the tropics (Fig. 7b). The intermediate ocean (300m-1200m) also contributes to $\Delta \mathrm{OHC}_{-\mathrm{IPO}}$ at mid and high-latitudes (Fig. 7c), with anomalies of the same sign as in the upper 300m. The OHC changes are

441 weaker below 1200m (Fig. 7d), and mostly located in the Southern Ocean, in contrast to
442 Meehl et al. (2011) who pointed to larger heat content variations in the deep ocean during
443 hiatus periods.

444

445 *4.3 Regional heat budget for the IPO-induced OHC changes*

446 We now investigate the contributions from surface fluxes, oceanic transport, and the
447 residue, as in Eq. (2), for ΔOHC_{-IPO}. Figure 8 shows this regionally-integrated budget for the
448 tropical Pacific, North Pacific (north of 31°N), Atlantic (including the Arctic), Southern
449 (south of 31°S), and Indian Ocean basins (basin boundaries are depicted in Figs 7 and 8e).
450 The residual in Eq. (2) (Fig. 8d) represents the contributions of parameterized diffusive lateral
451 mixing and changing sea ice heat content. This residual is in general close to zero or much
452 weaker than the dominant terms in the budget, so that OHC changes can be accounted for by
453 the sum of the surface heat uptake and ocean heat flux transport convergence.

454 We find that the anomalous surface heat uptake during the 1998-2012 IPO negative
455 phase (Fig. 8c) exclusively occurs in the tropical Pacific Ocean ($65\pm4 \times 10^{21}$ J), with other
456 basins experiencing either negligible IPO-induced surface fluxes (Atlantic, Southern Ocean)
457 or more moderate heat losses to the Atmosphere (Indian Ocean, North Pacific). Despite this
458 major heat input from the atmosphere, the tropical Pacific OHC hardly changes over the
459 1998-2012 period (Fig. 8a). The tropical Pacific surface heat uptake is indeed entirely
460 transferred to other basins. The ratio of the oceanic transports from the tropical Pacific (Fig.
461 8b and arrows in Fig. 8e) versus the surface heat uptake (Figs. 8c and 8e) shows that 53% of
462 the heat received at the surface of the tropical Pacific is transferred to the North Pacific, 26%
463 to the Indian Ocean, and 21% to the South Pacific. Overall, 65% of the global ΔOHC_{-IPO}
464 occurs in the Southern Ocean ($26\pm11 \times 10^{21}$ J, as illustrated in Fig. 8a), where the surface heat
465 loss is negligible (Fig. 8c). The ratio of oceanic heat transport (arrows in Fig. 8e) versus the

southern ocean ΔOHC_{-IPO} illustrates that 49% of the OHC increase is due to the heat transport across 31°S from the tropical Pacific, 32% is due to the heat transport from the Indian ocean, and 19% is due to the transport from the Atlantic Oceans. Despite receiving the largest heat transport from the tropical Pacific, the North Pacific experiences a smaller OHC increase than the Southern Ocean (40% of the global OHC increase), due to heat losses to the atmosphere ($13\pm3 \times 10^{21}$ J, see Fig. 8c and 8e). In the Indian Ocean, about half of the input of heat from the tropical Pacific is evacuated southward to the Southern Ocean via the Indonesian throughflow (Fig. 8e), with a relatively large heat quantity ($17\pm2 \times 10^{21}$ J) released back to the atmosphere. As a result, the Indian Ocean experiences little ΔOHC_{-IPO}. In the Atlantic, the IPO induces little changes in either atmospheric heat uptake or transport, with no significant ΔOHC_{-IPO} as a result, as will be discussed in section 5.

As expected from the surface temperature changes, the integrated ΔOHC_{-IPO} over the different basins diminishes in the upper 50m (Fig. 9a), except for the Southern Ocean. The dominant OHC increase occurs within 50-300m in the tropical Pacific (Fig. 9b). However, the OHC decreases below 300m in the tropical Pacific, producing a negligible OHC anomaly over the total water column. Conversely, the Southern Ocean and North Pacific OHC increase at all depths below 50m. This suggests that there is a global heat redistribution within the ocean, as previously found (Meehl et al., 2011; Chen and Tung, 2014; Liu et al. 2016a; Liu et al. 2016b), but here our experiments find a larger role of the Southern Ocean, with an OHC increase that remains important below 1200m.

Figure 10 shows the spatial distributions of the heat budget terms. ΔOHC_{-IPO} (Fig. 10a) is repeated from Fig. 7a, while Fig. 10b and 10c are the contributions from surface fluxes and ocean heat transport. Table 2 quantifies these contributions to the global and regional ΔOHC_{-IPO} using pattern regression: 68% of the global OHC changes attributable to the IPO are driven by the oceanic transport. The tropical Pacific is the only region with a dominant

491 effect of the surface heat uptake (72%). This surface heat uptake occurs mostly over the
492 western tropical Pacific (Fig. 10b), due to cold IPO-induced SST anomalies there (Fig. 5a),
493 which favor a downward surface net heat flux anomaly. Table 3 further illustrates that the
494 enhanced downward heat flux is mostly due to the reduced upward surface latent heat flux
495 and the increased downward surface shortwave radiation. The increased downward surface
496 shortwave radiation is weaker in clear-sky conditions, and is consistent with the reduced total
497 cloud cover. The Pacific heat uptake during negative IPO phases is expected to occur in the
498 central and eastern Pacific (e.g. Kosaka and Xie, 2013). The dominant heat uptake in the
499 western Pacific in our simulations is probably related to the cold tongue bias, which induces
500 IPO-related SST anomalies which are too strong and shifted westward (Fig. 5).

501 In the North Pacific, Indian, and Atlantic Oceans, ocean dynamics are the dominant
502 contributor to $\Delta \mathrm{OHC}_{-\mathrm{IPO}}$, with surface fluxes to the atmosphere acting as a negative feedback
503 (Fig. 10, Table 2). In particular, ocean heat transport changes explain the two bands of
504 $\Delta \mathrm{OHC}_{-\mathrm{IPO}}$ increase around 40° latitude in both hemispheres. This anomalous oceanic heat
505 transport convergence is mainly due to the eulerian transport, with only a small contribution
506 from the eddy bolus transport (not shown). In the following section, we will focus on the
507 mechanisms that explain the main IPO-induced ocean heat flux convergence seen in Figs. 8
508 and 10c.

509

510 *4.4 Mechanisms of IPO-induced ocean heat transport*

511 The W-FULL minus W-CLIM SLP difference has a characteristic pattern of La Niña
512 or negative IPO teleconnections during 1998-2012 (Fig. 11a), with positive SLP anomalies in
513 the Aleutian Low region and around 50°S in the Pacific sector of the Southern Ocean (e.g.
514 Trenberth and Caron, 2000) and negative SLP anomalies over the Amundsen Sea (Turner et
515 al. 2013). As a result, the W-FULL minus W-CLIM wind stresses (Figs. 11a and 12a) display

positive anomalies around 55°S and 55°N, which can be interpreted as the poleward shift of westerlies characteristic of La Niña conditions (e.g. Lu et al. 2008).

To investigate the associated Ekman response, we compute the Ekman transport and pumping (Gill, 1982). The Ekman response to the anomalous wind stress indeed reveals increased poleward transport at 31°N and 31°S at the edges of the domains used in Fig. 8 (see Fig 11b). The horizontal Ekman meridional transport converges around 40° latitude in both hemispheres (Figs 11b-c). The negative SLP anomaly over the Amundsen Sea, typical of negative IPO conditions (Fogt et al 2012; Clem and Renwick, 2015; Meehl et al. 2016), also yields Ekman flow divergence at 60°S in the Pacific basin. ΔOHC_{-IPO} (Fig. 11b) is consistent with the Ekman response, with downward Ekman pumping associated with positive ΔOHC_{-IPO} especially at 40°S, between South of Australia and South America and at 40°N in the North Pacific, and decreased OHC associated with upward Ekman pumping in the Amundsen Sea.

The influence of these processes is clearly seen in the anomalous W-FULL zonal-mean temperature change (Fig. 12b) that is dominated by the Pacific Ocean anomalies. The positive temperature anomalies at 40°S and 40°N penetrate downward into the ocean where the mean slope of the isopycnals is large (not shown), which enhances the heat penetration into the deeper layers through the mean flow. We also note an intensification of the shallow subtropical cells between 20°S and 20°N in the upper 400m of the ocean (see contours in Fig. 12b) as described in England et al. (2014), but these only lead to shallow temperature anomalies. Such anomalies are associated with the large OHC increase found at 50-300m in the tropical Pacific (see Fig. 9). A positive anomaly of the global meridional streamfunction is also found between 65°S and 50°S, as the Deacon cell intensifies and shifts southwards.

Llovel and Terray (2016) found a similar process when analysing Argo data and atmospheric reanalysis over the 2005-2014 period, but they could not attribute these observed

changes specifically to either climate change or natural variability. Using our experimental setup, we can quantify those two influences. Figure 12a shows the zonal-mean wind stress anomalies associated with the negative IPO phase (black line) and the anomalies simulated in W-CLIM (black dashed line). In W-CLIM, increasing greenhouse gases and decreasing stratospheric ozone yield positive wind stress anomalies around 50°S (Shindell and Schmidt, 2004). The IPO-related (i.e. W-FULL minus W-CLIM) anomalies are similar, but they are, however, larger and 10° further south. Similarly, we evaluate that the Southern Ocean heat storage occurs at a rate of 61.9 ± 5.6 10^{21} J $decade^{-1}$ in W-FULL over the negative IPO period, while it occurs at a rate of 44.5 ± 5.1 10^{21} J $decade^{-1}$ over the same period in W-CLIM. For comparison, the average rate for the Southern Ocean heat storage is 33.1 ± 2.5 (39.2 ± 2.9) 10^{21} J $decade^{-1}$ over 1979-2014 in W-CLIM (W-FULL, respectively). Therefore, external forcings have caused an accelerated Southern Ocean OHC increase during the negative IPO period (increased rate of 23.1 ± 4.3 %), but we find that these changes are smaller than those induced by tropical SSTs through atmospheric teleconnections (increase of 48.1 ± 8.6 %).

Overall, our results therefore suggest that, during negative IPO phases, ENSO teleconnections to the extratropical Pacific drive increased poleward Ekman heat transport through 31°S and N. The associated Ekman pumping induces heat subduction at 40° S and N in the intermediate water formation regions of both hemispheres. The heat subducted in the Southern Ocean is larger than that in the northern Pacific, reflecting the larger meridional temperature gradient and the larger oceanic area in the Southern Hemisphere.

5. Summary and discussion

5.1. Summary

In this study, we examine the OHC changes over the 1998-2012 period, during which global mean surface temperature displayed a reduced warming rate, which has been attributed to oceanic heat redistribution and enhanced heat uptake in the Pacific (Meehl et al., 2011; Kosaka and Xie, 2013; Fyfe and Gillett, 2014; Clement and DiNezio, 2014; Trenberth, 2015; Dai et al., 2015). To test this hypothesis, we prescribe the 1979–2014 tropical Pacific (20°N-20°S) surface wind stress in two ensembles with identical GHG, aerosol, and ozone forcing: one with climatological wind stress (W-CLIM), and the other with wind stress anomalies from ERA-Interim (W-FULL). As already explored in previous studies (England et al. 2014; Watanabe et al. 2014; Douville et al. 2015; Delworth et al. 2015; Thoma et al. 2015; Saenko et al. 2016), we find that this strategy is successful in constraining ENSO variations in the tropical Pacific and their decadal modulation, with an El Niño residual signature during 1979-1997 and a La Niña signature during 1998-2012. Atmospheric teleconnections also produce global air temperature and SLP patterns characteristic of a transition from a positive to a negative IPO phase. As a result, W-FULL also simulates the observed reduced rate in global surface warming during 1992–2012 (Gleisner et al. 2015).

The SST and OHC anomaly patterns during the negative IPO phase (1998-2012) are similar to the observed ones, which allows us to use our simulations to investigate OHC changes during this period. The W-CLIM minus W-FULL ensemble mean indeed isolates the effects of enhanced tropical Pacific wind stresses associated with the negative IPO phase. The IPO negative phase leads to a global heat redistribution, in accordance with previous studies (Meehl et al. 2011, 2013; England et al. 2014). Almost all the anomalous oceanic heat uptake occurs in the tropical Pacific. Part of this heat is exported to the Indian Ocean through the enhanced throughflow, but yields no OHC increase due to heat release to the atmosphere and enhanced southward transport across 31°S in this basin. The remainder of the tropical Pacific heat uptake is transported polewards within the ocean. The largest OHC increase

591 occurs at all depths in the Southern and North Pacific Oceans. The OHC increase is weaker
592 in the North Pacific as much of the heat is released back to the atmosphere in this region.
593 There is a strong heat convergence around 40°N and 40°S due to the teleconnections
594 associated with the cold tropical Pacific SST, producing enhanced poleward Ekman transport
595 across 31°N and 31°S, and Ekman convergence at 40° latitude in both hemispheres, as found
596 by Oke and England (2004). As a result, the OHC changes are strongly related to the Ekman
597 pumping patterns associated with IPO teleconnections. Recent simulations have also shown a
598 southward transport of ocean heat from the tropical Pacific during the 1998–2012 warming
599 slowdown (Oka and Watanabe 2017). Our experimental protocol allows us to attribute most
600 of this wind-driven OHC change to IPO-related teleconnections.
601
602 *5.2. Discussion*
603 It is important to acknowledge some limitations in our modeling. First, as mentioned
604 previously, IPSL-CM5A-LR, like many other models, displays SST anomalies in the tropical
605 Pacific that extend too far westward, which is linked to the equatorial Pacific cold tongue
606 bias (Li and Xie, 2014). This probably explains why the heat uptake occurs predominantly in
607 the western Pacific in our study, whereas it is generally expected to occur mostly in the
608 central/eastern Pacific (e.g. Tokinaga and Xie, 2012).
609 We have seen in our results that the W-FULL minus W-CLIM anomalous heat uptake
610 occurred almost exclusively during the 1998-2012 negative IPO period, with little sign of
611 anomalous heat uptake during the 1979-1997 positive IPO period. Why is there such an
612 asymmetry? As expected, the negative IPO is characterized by a negative SST anomaly and
613 the positive IPO by a positive SST anomaly in the tropical Pacific (Table 3). As a result, the
614 longwave, sensible and latent surface heat fluxes have opposite signs during these two
615 periods. However, the shortwave surface heat flux displays positive anomalies during both

phases. This can be related to the observed non-linearity of the shortwave flux associated with ENSO-related SST anomalies (Fig. 13b). During La Niñas, observations indicate a decrease in the incoming shortwave radiation, consistent with a stronger atmospheric inversion at the top of the planetary boundary layer, and increased low-level cloud coverage (Fig. 13b; Stephens, 2005). During El Niños, positive SST anomalies lead to atmospheric convection and increasing high and mid-level cloud coverage, which also reduce the surface shortwave radiation (Fig. 13b). Bellenger et al. (2014) have shown that most CMIP5 models have trouble reproducing this nonlinear behavior. This is also the case in the IPSL-CM5A model we use here, even though using prescribed wind stress improves this aspect of the model (Fig. 13a). The shortwave dependence on SST anomalies is reasonable during La Niñas, but the effect of warm SSTs onto shortwave surface heat flux is largely underestimated in the model. Due to this issue, we chose to only focus on the 1998-2012 negative IPO phase in the current study. Nevertheless, the observed asymmetry of the surface shortwave heat flux to SST suggests that there may also be some asymmetry in heat uptake between IPO positive and negative phases in the real world.

The model used in this study (IPSL-CM5A-LR) also displays a large climate sensitivity, with a rather strong TOA radiative imbalance compared to observations (Loeb et al., 2012; Allan et al., 2014, Johnson et al., 2016) or other models such as CCSM4 (Meehl et al., 2011) or CESM (Liu et al., 2016a). It likely that the cloud-related processes linked to this large sensitivity are also involved in the global TOA radiative imbalance and global OHC variations associated with the IPO. More work is needed to verify if the OHC changes related to the IPO found in this study are robust. This can be done through other pacemaker ensemble experiments with other models or analyses of the OHC modulation by the IPO phase in the CMIP5 preindustrial control runs.

640 Outside the Pacific, our simulations can also be used to reveal the influence of the
641 Pacific Ocean variability onto the Indian and Atlantic Oceans. Our results indicate a large
642 increase of the heat transport to the Indian Ocean during the negative IPO phase. This agrees
643 with several recent studies using both modeling and observations (Lee et al. 2015; Nieves et
644 al. 2015; Liu et al. 2016a). Despite this large heat transfer to the Indian Ocean via the
645 Indonesian throughflow, there is hardly any IPO-induced change in the Indian Ocean OHC
646 over the 1998-2012 period in our simulations, due to increased southward heat transport
647 across 31°S and heat released to the atmosphere through surface fluxes. Is this realistic? To
648 investigate this, we compare the sea-level changes attributable to the IPO (W-FULL minus
649 W-CLIM) to observed sea level over 1998-2012 in Fig. 14. The globally-averaged sea-level
650 signal has been subtracted to remove potential effects of changes in the cryosphere and land
651 storage (Greatbatch, 1994). The model underestimates the observed sea level rise in the
652 eastern and southeastern Indian Ocean. This region is directly connected to the western
653 Pacific via the Indonesian throughflow at decadal and multidecadal timescales (e.g. Feng et
654 al. 2004). The sea level anomalies at the equator in the western Pacific (where the
655 throughflow entrance is located) are also strongly underestimated relative to observations,
656 probably due to the cold tongue bias in the Pacific and associated westward shift of
657 equatorial easterly anomalies. There is thus probably an underestimation of the heat transfer
658 from the Pacific to the Indian Ocean. It is more difficult to gauge whether the southward
659 ocean transport across 31°S and the strong surface heat losses to the atmosphere in the model
660 (Fig. 8) are realistic or not.
661 The Atlantic Ocean is also influenced by the Pacific variability in W-FULL. The
662 1998–2012 Atlantic zonal-mean changes linked to the cold IPO phase are shown in Fig. 15.
663 The IPO-related signal in our simulation is weak in the Northern Atlantic. In contrast, Chen
664 and Tung (2014) find a large temperature increase over the whole north Atlantic from

665 observations, but they do not separate the IPO signal from that associated with anthropogenic
666 climate change. During the negative IPO, the Atlantic OHC increase is largely concentrated in
667 the first 1000m at 40°N, while OHC decreases between 50°N and 60°N, and at 15°N. These
668 changes are consistent with the SST anomalies (Fig. 5a) showing the typical SST tripole
669 driven by the positive NAO-like SLP anomalies occurring over the North Atlantic sector
670 (Figs. 3b and 11a). W-FULL also simulates a 0.6 Sv weaker Atlantic meridional overturning
671 circulation relative to W-CLIM (Fig. 15, contours), which is consistent with the fast Ekman-
672 driven barotropic oceanic response to a positive NAO (Eden and Willebrand, 2001). The
673 positive NAO-like anomalies in W-FULL are consistent with those arising from La Niña (or
674 negative IPO) teleconnections (Gastineau et al., 2013). In observations, the North Atlantic
675 SLP anomalies are not significant during 1998-2012 (see NAO trends in Table 1) and the
676 atmospheric internal variability dominates the decadal variability. Our results therefore agree
677 with a dominant role of the global heat redistribution induced by the negative IPO, with little
678 influence of the Atlantic Ocean, as found by Liu et al. (2016a, 2016b). Nevertheless, the
679 Atlantic variability might have influenced the Pacific Ocean through its impacts onto the
680 Walker circulation, as found by Li et al. (2016) or Ruprich-Robert et al. (2017), but this role
681 of the Atlantic Ocean cannot be addressed with our simulations.

682 Lastly, our working hypothesis is that external forcings have no impact on the Pacific
683 trade wind intensification during 1998-2012, so that we attribute the differences between the
684 results of W-FULL and W-CLIM entirely to IPO variability. However, some studies have
685 suggested that external forcing may have lead to a significant part of the observed trade wind
686 strengthening (Luo et al. 2012; Han et al. 2014; Kohyama et al., 2016; Dong and McPhaden
687 2017), in particular due to accelerated Indian Ocean warming. This is in contradiction to
688 other studies that indicate that anthropogenic climate change should drive a weakening of the
689 Walker circulation (e.g. Held and Soden, 2005; Kociuba and Power, 2015). Other studies

point to the Atlantic (Chikamoto et al. 2012; McGregor et al. 2014; Li et al. 2015; Kucharski et al. 2016) or to Pacific aerosols (Allen et al., 2015; Takahashi and Watanabe 2016; Smith et al., 2016) as the ultimate cause of the trade wind strengthening during recent decades. More research is hence probably needed to reach a consensus on the main cause of the trade wind strengthening during recent decades.

Despite these caveats, our experiments provide a robust assessment of the links between the cold IPO phase (be it purely occurring as internal variability or externally forced), the global surface temperature warming slowdown, and the large OHC increase in the Southern Ocean during the first decade of the 21st century. Our results point towards the role of tropical Pacific decadal variability, acting through an atmospheric stationary wave response, to change surface winds and Ekman transport and store heat in the Southern Ocean and North Pacific. We suggest that further modeling simulations would help clarify the link between the IPO and heat content increase in the Southern Ocean, to assess the model dependence of the processes, and to investigate if such links remain at eddy-permitting ocean resolution (Treguier et al., 2010).

Acknowledgments

This research was supported by the French National Research Agency under the program Facing Societal, Climate and Environmental Changes (MORDICUS project, grant ANR-13-SENV-0002). This work was granted access to the HPC resources of TGCC under the allocation 2015-017403 and 2016-017403 made by GENCI. This study also benefited from the IPSL mesocenter facility which is supported by CNRS, UPMC, Labex L-IPSL (funded by the ANR grant #ANR-10-LABX-0018 and by the European FP7 IS-ENES2 Grant #312979). We thank the ECMWF for providing the ERA-Interim reanalysis. The ECMWF

715 ORAS4 reanalysis was provided by the CliSAP-Integrated Climate Data Center at the
716 University of Hamburg. The AVISO SSH data were obtained from Marine Copernicus
717 service. The OISST dataset was provided by the NOAA/OAR/ESRL PSD, Boulder,
718 Colorado. The HadISST1 dataset was provided by the Met Office Hadley Centre. The
719 TropFlux dataset is produced under a collaboration between LOCEAN/IPSL/IRD and the
720 National Institute of Oceanography/CSIR, and relies on ERA-Interim and ISCCP data.
721
722
723 **References**
724 Abraham JP, Baringer M, Bindoff NL, Boyer T, Cheng LJ, Church JA, Conroy JL, et al.
725 (2013) A Review of Global Ocean Temperature Observations: Implications for Ocean
726 Heat Content Estimates and Climate Change. *Reviews of Geophysics* 51 (3):450–483.
727 https://doi.org/10.1002/rog.20022.
728 Allan RP, Liu C, Loeb NG, Palmer MD, Roberts M, Smith D, and Vidale P.-L. (2014)
729 Changes in Global Net Radiative Imbalance 1985–2012. *Geophysical Research Letters*
730 41 (15):5588–97. https://doi.org/10.1002/2014GL060962.
731 Allen RJ, Evan AT, and Booth BBB (2015) Interhemispheric Aerosol Radiative Forcing and
732 Tropical Precipitation Shifts during the Late Twentieth Century. *Journal of Climate* 28
733 (20):8219–46. https://doi.org/10.1175/JCLI-D-15-0148.1.
734 Andrews T, Gregory JM, Webb MJ, and Taylor KE (2012) Forcing, Feedbacks and Climate
735 Sensitivity in CMIP5 Coupled Atmosphere-Ocean Climate Models. *Geophysical*
736 *Research Letters* 39 (9):L09712. https://doi.org/10.1029/2012GL051607.
737 Balmaseda MA, Trenberth KE, and Källén E (2013) Distinctive Climate Signals in Reanalysis
738 of Global Ocean Heat Content. *Geophysical Research Letters* 40 (9):1754–1759.
739 https://doi.org/10.1002/grl.50382.

Balmaseda MA, Mogensen K, and Weaver AT (2013) Evaluation of the ECMWF Ocean Reanalysis System ORAS4. *Quarterly Journal of the Royal Meteorological Society* 139 (674):1132–1161. https://doi.org/10.1002/qj.2063.

Bellenger H, Guilyardi E, Leloup J, Lengaigne M, and Vialard J (2014) ENSO Representation in Climate Models: From CMIP3 to CMIP5. *Climate Dynamics* 42 (7–8):1999–2018.

Bindoff NL, Stott PA, AchutaRao KM, Allen MR, Gillett N, Gutzler D, Hansingo K, et al. (2013) Detection and Attribution of Climate Change: From Global to Regional. In Climate Change 2013: The Physical Science Basis. Contribution of Working Group I to the Fifth Assessment Report of the Intergovernmental Panel on Climate Change, 867–952. Cambridge: Cambridge University Press.

de Boisséson E, Balmaseda MA, Abdalla S, Källén E, and Janssen PEM (2014) How Robust Is the Recent Strengthening of the Tropical Pacific Trade Winds? *Geophysical Research Letters* 41 (12):4398–4405. https://doi.org/10.1002/2014GL060257.

Bretherton CS, Widmann M, Dymnikov VP, Wallace JM, and Bladé, I (1999). The effective number of spatial degrees of freedom of a time-varying field. *Journal of climate*, *12*(7), 1990-2009.

Brient F, and Bony S (2013) Interpretation of the Positive Low-Cloud Feedback Predicted by a Climate Model under Global Warming. *Climate Dynamics* 40 (9–10):2415–31. https://doi.org/10.1007/s00382-011-1279-7.

Cattiaux J, Douville H, and Peings Y (2013) European Temperatures in CMIP5: Origins of Present-Day Biases and Future Uncertainties. *Climate Dynamics* 41 (11–12):2889–2907. https://doi.org/10.1007/s00382-013-1731-y.

Chen X, and Tung K-K (2014). Varying Planetary Heat Sink Led to Global-Warming Slowdown and Acceleration. *Science* 345 (6199):897–903. https://doi.org/10.1126/science.1254937.

765 Chen X, and Tung K-K (2016). Correspondence: Variations in Ocean Heat Uptake during the
766 Surface Warming Hiatus. *Nature Communications* 7 (August):12541.
767 https://doi.org/10.1038/ncomms12541.
768 Cheng L, Trenberth KE, Fasullo J, Boyer T, Abraham J and Zhu J. (2017). Improved
769 estimates of ocean heat content from 1960 to 2015. *Science Advances*, *3*(3),
770 e1601545. https://doi.org/10.1126/sciadv.1601545.
771 Chikamoto Y, Kimoto M, Watanabe M, Ishii M, and Mochizuki T (2012). Relationship
772 between the Pacific and Atlantic Stepwise Climate Change during the 1990s.
773 *Geophysical Research Letters* 39 (21):L21710. https://doi.org/10.1029/2012GL053901.
774 Choi J-W, Kim I-G, Kim J-Y, and Park C-H (2016) The Recent Strengthening of Walker
775 Circulation. *SOLA* 12:96–99. https://doi.org/10.2151/sola.2016-022.
776 Clem KR and Renwick JA (2015). Austral spring Southern Hemisphere circulation and
777 temperature changes and links to the SPCZ. *Journal of Climate*, *28*(18), 7371-7384.
778 https://doi.org/10.1175/JCLI-D-15-0125.1.
779 Clement A, and DiNezio P (2014) The Tropical Pacific Ocean—Back in the Driver's Seat?"
780 *Science* 343 (6174):976–78. https://doi.org/10.1126/science.1248115.
781 Dai A, Fyfe JC, Xie S-P, and Dai X (2015) Decadal Modulation of Global Surface
782 Temperature by Internal Climate Variability. *Nature Climate Change* 5 (6):555–59.
783 https://doi.org/10.1038/nclimate2605.
784 Dee DP, Uppala SM, Simmons AJ, Berrisford P, Poli P, Kobayashi S, Andrae U, et al. (2011)
785 The ERA‐Interim Reanalysis: Configuration and Performance of the Data Assimilation
786 System. *Quarterly Journal of the Royal Meteorological Society* 137 (656):553–97.
787 https://doi.org/10.1002/qj.828.

788 Delworth TL, Zeng F, Rosati A, Vecchi GA, and Wittenberg AT (2015) A Link between the
789 Hiatus in Global Warming and North American Drought. *Journal of Climate* 28
790 (9):3834–45. https://doi.org/10.1175/JCLI-D-14-00616.1.
791 Deser C, Alexander MA, Xie S-P, and Phillips AS (2010). Sea surface temperature
792 variability: Patterns and mechanisms. *Annual review of marine science*, *2*, 115-143.
793 Dong L, and McPhaden MJ. 2016. "Why Has the Relationship between Indian and Pacific
794 Ocean Decadal Variability Changed in Recent Decades?" *Journal of Climate* 30
795 (6):1971–83. https://doi.org/10.1175/JCLI-D-16-0313.1.
796 Douville HA, Voldoire A, and Geoffroy O (2015) The Recent Global Warming Hiatus: What
797 Is the Role of Pacific Variability? *Geophysical Research Letters* 42 (3):2014GL062775.
798 https://doi.org/10.1002/2014GL062775.
799 Drijfhout S, Blaker AT, Josey SA, Nurser AJG, Sinha B, and Balmaseda MA (2014) Surface
800 Warming Hiatus Caused by Increased Heat Uptake across Multiple Ocean Basins.
801 *Geophysical Research Letters* 41 (22):7868–74.
802 https://doi.org/10.1002/2014GL061456.
803 Drijfhout S, Van Oldenborgh GJ, and Cimatoribus A (2012). Is a decline of AMOC causing
804 the warming hole above the North Atlantic in observed and modeled warming patterns?
805 *Journal of Climate*, *25*(24), 8373–8379.
806 Dufresne J-L, Foujols M-A, Denvil S, Caubel A, Marti O, Aumont O, Balkanski Y, et al.
807 (2013) Climate Change Projections Using the IPSL-CM5 Earth System Model: From
808 CMIP3 to CMIP5. *Climate Dynamics* 40 (9–10):2123–65.
809 https://doi.org/10.1007/s00382-012-1636-1.
810 Easterling DR and Wehner MF (2009) Is the climate warming or cooling? *Geophysical*
811 *Research Letters*, *36*(8).

812 Eden C and Willebrand J (2001) Mechanism of interannual to decadal variability of the North
813 Atlantic circulation. *Journal of Climate*, *14*(10), 2266-2280.
814 England MH, McGregor S, Spence P, Meehl GA, Timmermann A, Cai W, Sen Gupta A,
815 McPhaden MJ, Purich A, and Santoso A (2014) Recent Intensification of Wind-Driven
816 Circulation in the Pacific and the Ongoing Warming Hiatus. *Nature Climate Change* 4
817 (3):222–27. https://doi.org/10.1038/nclimate2106.
818 Feng M, Li Y, and Meyers G (2004) Multidecadal variations of Fremantle sea level: Footprint
819 of climate variability in the tropical Pacific, *Geophysical Research Letter*, 31, L16302,
820 doi:10.1029/2004GL019947.
821 Fichefet T, and Maqueda MA (1997) Sensitivity of a Global Sea Ice Model to the Treatment
822 of Ice Thermodynamics and Dynamics. *Journal of Geophysical Research: Oceans* 102
823 (C6):12609–46. https://doi.org/10.1029/97JC00480.
824 Fleming LE, and Anchukaitis KJ (2016) North Pacific Decadal Variability in the CMIP5 Last
825 Millennium Simulations. *Climate Dynamics* 47 (12):3783–3801.
826 https://doi.org/10.1007/s00382-016-3041-7.
827 Fogt RL, Wovrosh AJ, Langen RA and Simmonds I (2012). The characteristic variability and
828 connection to the underlying synoptic activity of the Amundsen‐Bellingshausen Seas
829 Low. *Journal of Geophysical Research: Atmospheres*, *117*(D7).
830 https://doi.org/10.1029/2011JD017337.
831 Forster PM, Andrews T, Good P, Gregory JM, Jackson LS, and Zelinka M. (2013) Evaluating
832 Adjusted Forcing and Model Spread for Historical and Future Scenarios in the CMIP5
833 Generation of Climate Models. *Journal of Geophysical Research: Atmospheres* 118
834 (3):1139–50. https://doi.org/10.1002/jgrd.50174.
835 Foster G, and Rahmstorf S (2011) Global Temperature Evolution 1979–2010. *Environmental*
836 *Research Letters* 6 (4):044022. https://doi.org/10.1088/1748-9326/6/4/044022.

837 Frankignoul C, Gastineau G, and Kwon Y-O (2017) Estimation of the SST Response to
838 Anthropogenic and External Forcing and Its Impact on the Atlantic Multidecadal
839 Oscillation and the Pacific Decadal Oscillation. *Journal of Climate* 30 (24):9871–95.
840 https://doi.org/10.1175/JCLI-D-17-0009.1.
841 Fyfe JC, and Gillett NP (2014) Recent Observed and Simulated Warming. *Nature Climate*
842 *Change* 4 (3):150–51. https://doi.org/10.1038/nclimate2111.
843 Gastineau G, D'Andrea F, and Frankignoul C (2013) Atmospheric Response to the North
844 Atlantic Ocean Variability on Seasonal to Decadal Time Scales. *Climate Dynamics* 40
845 (9–10):2311–2330.
846 Gill, AE. *Atmosphere—ocean dynamics*. Elsevier, 1982.
847 Gleisner H, Thejll P, Christiansen B, and Nielsen JK (2015) Recent Global Warming Hiatus
848 Dominated by Low-Latitude Temperature Trends in Surface and Troposphere Data.
849 *Geophysical Research Letters* 42 (2):2014GL062596.
850 https://doi.org/10.1002/2014GL062596.
851 Greatbatch RJ (1994) A note on the representation of steric sea level in models that conserve
852 volume rather than mass. *Journal of Geophysical Research: Oceans*, *99*(C6), 12767-
853 12771.
854 Han W, Meehl GA, Hu A, Alexander MA, Yamagata T, Yuan D, et al. (2014) Intensification
855 of decadal and multi-decadal sea level variability in the western tropical Pacific
856 during recent decades. *Climate dynamics*, **43,** 1357-1379.
857 Hansen J, Sato M, Kharecha P, and von Schuckmann, K (2011). Earth's energy imbalance
858 and implications. *Atmospheric Chemistry and Physics*, *11*(24), 13421–13449.
859 https://doi.org/10.5194/acp-11-13421-2011

860 Henley BJ, Gergis J, Karoly DJ, Power S, Kennedy J, and Folland CK (2015) A Tripole Index
861 for the Interdecadal Pacific Oscillation. *Climate Dynamics*, 1–14.
862 https://doi.org/10.1007/s00382-015-2525-1.
863 Hobbs W, Palmer MD, and Monselesan D (2016) An Energy Conservation Analysis of
864 Ocean Drift in the CMIP5 Global Coupled Models. *Journal od Climate,* 29, 1639–
865 1653, https://doi.org/10.1175/JCLI-D-15-0477.1
866 Horel JD, and Wallace JM (1981) Planetary-Scale Atmospheric Phenomena Associated with
867 the Southern Oscillation. *Monthly Weather Review* 109 (4):813–29.
868 Hourdin F, Foujols M-A, Codron F, Guemas V, Dufresne J-L, Bony S, Denvil S, et al. (2013)
869 Impact of the LMDZ Atmospheric Grid Configuration on the Climate and Sensitivity of
870 the IPSL-CM5A Coupled Model. *Climate Dynamics*, 40 (9–10):2167–2192.
871 Hung M-P, Lin J-L, Wang W, Kim D, Shinoda T, and Weaver SJ (2013). MJO and
872 Convectively Coupled Equatorial Waves Simulated by CMIP5 Climate Models. *Journal*
873 *of Climate* 26 (17):6185–6214. https://doi.org/10.1175/JCLI-D-12-00541.1.
874 Johnson G, Lyman J and Loeb N (2016). Improving estimates of Earth's energy
875 imbalance. *Nature Climate Change*, *6*(7), 639-640.
876 Kociuba G, and Power SB (2015) Inability of CMIP5 Models to Simulate Recent
877 Strengthening of the Walker Circulation: Implications for Projections. *Journal of*
878 *Climate* 28 (1):20–35. https://doi.org/10.1175/JCLI-D-13-00752.1.
879 Kohyama T, Hartmann DL, and Battisti SD (2017) La Niña–like Mean-State Response to
880 Global Warming and Potential Oceanic Roles. *Journal of Climate*, 30, 4207-4225.
881 https://doi.org/10.1175/JCLI-D-16-0441.1.
882 Kosaka Y, and Xie S-P (2013) Recent Global-Warming Hiatus Tied to Equatorial Pacific
883 Surface Cooling. *Nature* 501 (7467):403–7. https://doi.org/10.1038/nature12534.

884 Krinner G, Viovy N, de Noblet-Ducoudré N, Ogée J, Polcher J, Friedlingstein P, Ciais P,
885 Sitch S, and Prentice IC (2005) A Dynamic Global Vegetation Model for Studies of the
886 Coupled Atmosphere-Biosphere System. *Global Biogeochemical Cycles* 19
887 (1):GB1015. https://doi.org/10.1029/2003GB002199.
888 Kucharski F, Ikram F, Molteni F, Farneti R, Kang I-S, No H-H, King MP, Giuliani G, and
889 Mogensen K (2016) Atlantic Forcing of Pacific Decadal Variability. *Climate Dynamics*
890 46 (7–8):2337–51. https://doi.org/10.1007/s00382-015-2705-z.
891 Kumar BP, Vialard J, Lengaigne M, Murty VSN, and McPhaden MJ (2012) TropFlux: Air-
892 Sea Fluxes for the Global Tropical Oceans—description and Evaluation. *Climate*
893 *Dynamics* 38 (7–8):1521–43. https://doi.org/10.1007/s00382-011-1115-0.
894 Lee S-K, Park W, Baringer MO, Gordon AL, Huber B, and Liu Y (2015) Pacific Origin of the
895 Abrupt Increase in Indian Ocean Heat Content during the Warming Hiatus. *Nature*
896 *Geoscience* 8 (6):445–49. https://doi.org/10.1038/ngeo2438.
897 Leuliette EW (2015) The Balancing of the Sea-Level Budget. *Current Climate Change*
898 *Reports* 1 (3):185–91. https://doi.org/10.1007/s40641-015-0012-8.
899 Li J, Sun C, and Jin F-F (2013) NAO implicated as a predictor of Northern Hemisphere
900 mean temperature multidecadal variability, *Geophys. Res. Lett.*, 40, 5497–5502,
901 *doi:*10.1002/2013GL057877.
902 Li G, and Xie S-P (2014). Tropical biases in CMIP5 multimodel ensemble: The excessive
903 equatorial Pacific cold tongue and double ITCZ problems. *Journal of Climate*, *27*(4),
904 1765–1780.
905 Li X, Xie S-P, Gille S-T, and Yoo C (2015) Atlantic-Induced Pan-Tropical Climate Change
906 over the Past Three Decades. *Nature Climate Change,* advance online publication.
907 https://doi.org/10.1038/nclimate2840.

908 Liu W, Xie S-P, and Lu J (2016a) Tracking Ocean Heat Uptake during the Surface Warming
909 Hiatus. *Nature Communications* 7 (March):10926.
910 https://doi.org/10.1038/ncomms10926.
911 Liu W, Xie S-P, and Lu J (2016b) Correspondence: Reply to: 'Correspondence ; Tracking
912 Ocean Heat Uptake during the Surface Warming Hiatus'. *Nature Communications* 7
913 (August):12542. https://doi.org/10.1038/ncomms12542.
914 Llovel W, and Terray L (2016) Observed Southern Upper-Ocean Warming over 2005–2014
915 and Associated Mechanisms. *Environmental Research Letters* 11 (12):124023.
916 https://doi.org/10.1088/1748-9326/11/12/124023.
917 Loeb NG, Lyman JM, Johnson GC, Allan RP, Doelling DR, Wong T, Soden BJ, and
918 Stephens GL (2012) Observed Changes in Top-of-the-Atmosphere Radiation and
919 Upper-Ocean Heating Consistent within Uncertainty. *Nature Geoscience* 5 (2):110–13.
920 https://doi.org/10.1038/ngeo1375.
921 Lu J, Chen G, and Frierson DMW (2008) Response of the Zonal Mean Atmospheric
922 Circulation to El Nino versus Global Warming. *Journal of Climate* 21 (22):5835–51.
923 https://doi.org/10.1175/2008JCLI2200.1.
924 Luo JJ, Sasaki W and Masumoto Y (2012) Indian Ocean warming modulates Pacific climate
925 change. *Proceedings of the National Academy of Sciences*, *109*(46), 18701-18706.
926 Lyman JM (2012) Estimating Global Energy Flow from the Global Upper Ocean. *Surveys in*
927 *Geophysics* 33 (3–4):387–93. https://doi.org/10.1007/s10712-011-9167-6.
928 Madec G (2008) NEMO Ocean Engine. Publication - Report. http://nora.nerc.ac.uk/164324/.
929 Maury P, Lott F, Guez L, and Duvel J-P (2013) Tropical Variability and Stratospheric
930 Equatorial Waves in the IPSLCM5 Model. *Climate Dynamics* 40 (9–10):2331–2344.
931 McGregor S, Timmermann A, Stuecker MF, England MH, Merrifield M, Jin F-F, and
932 Chikamoto Y (2014) Recent Walker Circulation Strengthening and Pacific Cooling

933 Amplified by Atlantic Warming. *Nature Climate Change* 4 (10):888–92.
934 https://doi.org/10.1038/nclimate2330.
935 McPhaden MJ, Zebiak SE, and Glantz MH (2006). ENSO as an integrating concept in earth
936 science. *science*, *314*(5806), 1740-1745.
937 Medhaug I, Stolpe MB, Fischer EM, and Knutti R (2017) Reconciling Controversies about
938 the 'Global Warming Hiatus. *Nature* 545 (7652):41–47.
939 https://doi.org/10.1038/nature22315.
940 Meehl GA, Arblaster JM, Fasullo JT, Hu A, and Trenberth KE (2011) Model-Based Evidence
941 of Deep-Ocean Heat Uptake during Surface-Temperature Hiatus Periods. *Nature*
942 *Climate Change* 1 (7):360–64. https://doi.org/10.1038/NCLIMATE1229.
943 Meehl GA, Hu A, Arblaster JM, Fasullo J, and Trenberth KE (2013) Externally Forced and
944 Internally Generated Decadal Climate Variability Associated with the Interdecadal
945 Pacific Oscillation. *Journal of Climate* 26 (18):7298–7310.
946 https://doi.org/10.1175/JCLI-D-12-00548.1.
947 Meehl GA, Arblaster JM, Bitz CM, Chung CT and Teng H (2016) Antarctic sea-ice
948 expansion between 2000 and 2014 driven by tropical Pacific decadal climate variability.
949 *Nature Geoscience*, *9*(8), 590-595. https://doi:10.1038/ngeo2751.
950 Nerem RS, Chambers DP, Choe C, and Mitchum GT (2010) Estimating Mean Sea Level
951 Change from the TOPEX and Jason Altimeter Missions. *Marine Geodesy* 33
952 (sup1):435–46. https://doi.org/10.1080/01490419.2010.491031.
953 Nidheesh AG, Lengaigne M, Vialard J, Izumo T, Unnikrishnan AS, and Cassou C (2017)
954 Influence of ENSO on the Pacific Decadal Oscillation in CMIP Models. *Climate*
955 *Dynamics*, February, 1–18. https://doi.org/10.1007/s00382-016-3514-8.
956 Nieves V, Willis JK, and Patzert WC (2015). Recent Hiatus Caused by Decadal Shift in Indo-
957 Pacific Heating. *Science* 349 (6247):532–35. https://doi.org/10.1126/science.aaa4521.

Oka A, and Watanabe M (2017) The Post-2002 Global Surface Warming Slowdown Caused by the Subtropical Southern Ocean Heating Acceleration. *Geophysical Research Letters*, 2016GL072184. https://doi.org/10.1002/2016GL072184.

Oke PR, and England MH (2004) Oceanic Response to Changes in the Latitude of the Southern Hemisphere Subpolar Westerly Winds. *Journal of Climate* 17 (5):1040–54.

Power ST, Casey T, Folland C, Colman A, and Mehta V (1999) Inter-Decadal Modulation of the Impact of ENSO on Australia. *Climate Dynamics* 15 (5):319–24. https://doi.org/10.1007/s003820050284.

Raphael MN, Marshall GJ, Turner J, Fogt RL, Schneider D, Dixon DA, Hosking JS, Jones JM, and Hobbs WR (2016) The Amundsen Sea Low: Variability, Change, and Impact on Antarctic Climate. *Bulletin of the American Meteorological Society* 97 (1):111–21. https://doi.org/10.1175/BAMS-D-14-00018.1.

Rayner NA, Parker DE, Horton EB, Folland CK, Alexander LV, Rowell DP, Kent EC, Kaplan A (2003) Global analyses of sea surface temperature, sea ice, and night marine air temperature since the late nineteenth century Journal of Geophysical Research 108 (D14): 4407, https://doi.org/10.1029/2002JD002670.

Reynolds RW, Rayner NA, Smith TM, Stokes DC, and Wang WQ (2002) An Improved in Situ and Satellite SST Analysis for Climate. *Journal of Climate* 15 (13):1609–25.

Ridley DA, Solomon S, Barnes JE, Burlakov VD, Deshler T, Dolgii SI, Herber AB, et al. (2014) Total Volcanic Stratospheric Aerosol Optical Depths and Implications for Global Climate Change. *Geophysical Research Letters* 41 (22):2014GL061541. https://doi.org/10.1002/2014GL061541.

Roemmich D, Church J, Gilson J, Monselesan D, Sutton P, and Wijffels S (2015) Unabated Planetary Warming and Its Ocean Structure since 2006. *Nature Climate Change* 5 (3):240–45. https://doi.org/10.1038/nclimate2513.

983 Ruprich-Robert Y, Msadek R, Castruccio F, Yeager S, Delworth T, and Danabasoglu G
984 (2017). Assessing the climate impacts of the observed Atlantic multidecadal variability
985 using the GFDL CM2. 1 and NCAR CESM1 global coupled models. *Journal of*
986 *Climate*, *30*(8), 2785-2810. https://doi.org/10.1175/JCLI-D-16-0127.1
987 Saenko OA, Fyfe JC, Swart NC, Lee WG, and England MH (2016) Influence of Tropical
988 Wind on Global Temperature from Months to Decades. *Climate Dynamics* 47 (7–
989 8):2193–2203. https://doi.org/10.1007/s00382-015-2958-6.
990 Santer BD, Wigley TML, Boyle JS, Gaffen DJ, Hnilo JJ, Nychka D, Parker DE, and Taylor
991 KE (2000) Statistical Significance of Trends and Trend Differences in Layer-Average
992 Atmospheric Temperature Time Series. *Journal of Geophysical Research: Atmospheres*
993 105 (D6):7337–56. https://doi.org/10.1029/1999JD901105.
994 Santer BD, Bonfils C, Painter JF, Zelinka MD, Mears C, Solomon S, Schmidt GA, et al.
995 (2014) Volcanic Contribution to Decadal Changes in Tropospheric Temperature. *Nature*
996 *Geoscience* 7 (3):185–89. https://doi.org/10.1038/ngeo2098.
997 Sarachik ES, and Cane MA (2010). The El Niño-Southern Oscillation Phenomenon. 1st
998 edition. Cambridge: Cambridge University Press.
999 Sato M, Hansen JE, McCormick MP, and Pollack JB (1993). Stratospheric Aerosol Optical
1000 Depths, 1850–1990. *Journal of Geophysical Research: Atmospheres* 98 (D12):22987–
1001 94. https://doi.org/10.1029/93JD02553.
1002 Shindell DT and Schmidt GA (2004) Southern Hemisphere climate response to ozone
1003 changes and greenhouse gas increases. *Geophysical Research Letters, 31*(18).
1004 Smith DM, Allan RP, Coward AC, Eade R, Hyder P, Liu C, Loeb NG, Palmer MD, Roberts
1005 CD, and Scaife AA (2015) Earth's Energy Imbalance since 1960 in Observations and
1006 CMIP5 Models. *Geophysical Research Letters* 42 (4):2014GL062669.
1007 https://doi.org/10.1002/2014GL062669.

1008 Smith DM, Booth BB, Dunstone NJ, Eade R, Hermanson L, Jones GS, Scaife AA, Sheen KL,
1009 and Thompson V (2016). Role of volcanic and anthropogenic aerosols in the recent
1010 global surface warming slowdown. *Nature Climate Change*, *6*(10), 936.
1011 https://doi:10.1038/nclimate3058.
1012 Solomon S, Daniel JS, Neely RR, Vernier JP, Dutton EG, and Thomason LW (2011) The
1013 Persistently Variable 'Background' Stratospheric Aerosol Layer and Global Climate
1014 Change. *Science* 333 (6044):866–70. https://doi.org/10.1126/science.1206027.
1015 Stephens GL (2005). Cloud feedbacks in the climate system: A critical review. *Journal of*
1016 *climate*, *18*(2), 237-273.
1017 Sterl A, van Oldenborgh GJ, Hazeleger W and Burgers G (2007) On the robustness of ENSO
1018 teleconnections. *Climate Dynamics*, *29*(5), 469-485.
1019 Stouffer RJ, Manabe S, and Bryan K (1989) Interhemispheric Asymmetry In Climate
1020 Response To A Gradual Increase Of Atmospheric CO2. *Nature* 342 (6250):660–62.
1021 Takahashi C, and Watanabe M (2016) Pacific Trade Winds Accelerated by Aerosol Forcing
1022 over the Past Two Decades. *Nature Climate Change* advance online publication (April).
1023 https://doi.org/10.1038/nclimate2996.
1024 Taylor KE, Stouffer RJ, and Meehl GA (2012) An Overview of CMIP5 and the Experiment
1025 Design. *Bulletin of the American Meteorological Society* 93 (4):485–98.
1026 https://doi.org/10.1175/BAMS-D-11-00094.1.
1027 Thoma M, Greatbatch RJ, Kadow C, and Gerdes R (2015) Decadal Hindcasts Initialized
1028 Using Observed Surface Wind Stress: Evaluation and Prediction out to 2024.
1029 *Geophysical Research Letters* 42 (15):2015GL064833.
1030 https://doi.org/10.1002/2015GL064833.

1031 Tréguier A-M, Le Sommer J, Molines J-M, and De Cuevas B (2010). Response of the
1032 Southern Ocean to the Southern Annular Mode: Interannual variability and
1033 multidecadal trend. *Journal of Physical Oceanography*, *40*(7), 1659‑1668.
1034 Trenberth KE, Jones PD, Ambenje P, Bojariu R, Easterling D, Tank AK, Parker D,
1035 Rahimzadeh F, Renwick JA, and Rusticucci M (2007) Observations: Atmospheric
1036 Surface and Climate Change. In Climate Change 2007: The Physical Science Basis,
1037 235–336.
1038 Trenberth KE (2015) Has There Been a Hiatus? *Science* 349 (6249):691–92.
1039 https://doi.org/10.1126/science.aac9225.
1040 Trenberth KE, Branstator GW, Karoly D, Kumar A, Lau N-C, and Ropelewski C (1998)
1041 Progress during TOGA in Understanding and Modeling Global Teleconnections
1042 Associated with Tropical Sea Surface Temperatures. *Journal of Geophysical Research:*
1043 *Oceans* 103 (C7):14291–324. https://doi.org/10.1029/97JC01444.
1044 Trenberth KE, and Caron JM (2000). The Southern Oscillation revisited: Sea level pressures,
1045 surface temperatures, and precipitation. *Journal of Climate*, *13*(24), 4358-4365.
1046 Trenberth KE, Fasullo JT, and Balmaseda MA (2014) Earth's Energy Imbalance. *Journal of*
1047 *Climate* 27 (9):3129–44. https://doi.org/10.1175/JCLI-D-13-00294.1.
1048 Trenberth KE, Fasullo JT, Branstator G, and Phillips AS (2014) Seasonal Aspects of the
1049 Recent Pause in Surface Warming. *Nature Climate Change* 4 (10):911–16.
1050 https://doi.org/10.1038/nclimate2341.
1051 Trenberth KE, Fasullo JT and Kiehl J (2009). Earth's Global Energy Budget. *Bulletin of the*
1052 *American Meteorological Society*, *90*(3), 311‑323.
1053 https://doi.org/10.1175/2008BAMS2634.1
1054 Trenberth KE, and Hurrell JW (1994) Decadal Atmosphere-Ocean Variations in the Pacific.
1055 *Climate Dynamics* 9 (6):303–19. https://doi.org/10.1007/BF00204745.

1056 Turner J, Phillips T, Hosking JS, Marshall GJ and Orr A (2013) The Amundsen Sea low.
1057 *International journal of climatology*, *33*(7), 1818-1829.
1058 Vecchi GA and Soden BJ (2007). Global warming and the weakening of the tropical
1059 circulation. *Journal of Climate*, *20*(17), 4316-4340.
1060 Vecchi GA, Soden BJ, Wittenberg AT, Held IM, Leetmaa A, and Harrison MJ (2006)
1061 Weakening of Tropical Pacific Atmospheric Circulation Due to Anthropogenic Forcing.
1062 *Nature* 441 (7089):73–76. https://doi.org/10.1038/nature04744.
1063 Watanabe M, Shiogama H, Tatebe H, Hayashi M, Ishii M, and Kimoto M (2014)
1064 Contribution of Natural Decadal Variability to Global Warming Acceleration and
1065 Hiatus. *Nature Climate Change* 4 (10):893–97. https://doi.org/10.1038/nclimate2355.
1066 Yan X-H, Boyer T, Trenberth K, Karl TR, Xie S-P, Nieves V, Tung K-K, and Roemmich D.
1067 (2016) The Global Warming Hiatus: Slowdown or Redistribution? *Earth's Future* 4
1068 (11):2016EF000417. https://doi.org/10.1002/2016EF000417.
1069 Zhang Y, Wallace JM, and Battisti DS (1997) ENSO-like Interdecadal Variability: 1900–93.
1070 *Journal of Climate* 10 (5):1004–20.
1071

Table 1:1992–2012 trends of different climate indices associated with the IPO transition from the positive to the negative phase. The 95% confidence intervals are also given. Note that the confidence intervals are calculated differently for the models and observations. See Section 2.5 and 2.6 for details.

	Observation (ERA-Interim/OISST/ORAS4)	W-FULL	W-CLIM
Niño 3.4 SST	-0.29±0.47 °C dec^{-1}	-0.78±0.02 °C dec^{-1}	0.48±0.02 °C dec^{-1}
W–E thermocline tilt	17.7±12.0 m dec^{-1}	21.5±0.1 m dec^{-1}	-0.7±0.1 m dec^{-1}
IPO TPI SST	-0.50±0.4 °C dec^{-1}	-1.0±0.04 °C dec^{-1}	0.08±0.04 °C dec^{-1}
Global mean T2m	0.17±0.08 °C dec^{-1}	0.26±0.01 °C dec^{-1}	0.47±0.02 °C dec^{-1}
Pacific ΔSLP	0.61±0.59 hPa dec^{-1}	0.82±0.03 hPa dec^{-1}	-0.06±0.03 hPa dec^{-1}
North Pacific SLP	0.78±0.34 hPa dec^{-1}	1.45±0.16 hPa dec^{-1}	-0.10±0.20 hPa dec^{-1}
Amundsen Sea SLP	-1.08±1.11 hPa dec^{-1}	-1.34±0.53 hPa dec^{-1}	0.16±0.37 hPa dec^{-1}
NAO	-1.10±1.20 dec^{-1}	0.98±0.14 dec^{-1}	0.49±0.26 dec^{-1}

Table 2. Pattern regression (unitless) of the ocean surface heat uptake (first term in the r.h.s of Eq. (2)) and ocean heat flux convergence (second term in the r.h.s of Eq. (2)) during the 1998-2012 period onto ΔOHC_{-IPO} (l.h.s. of Eq. (2)). The two pattern regression coefficients sum to 1.0 by construction, and quantify the relative contributions of surface-flux and circulation-induced OHC changes to the total.

	Global	PacT	PacN	SO	Ind	Atl
Regression heat uptake onto OHC	0.32	0.72	-0.74	0.16	-0.64	-0.29
Regression ocean heat flux convergence onto OHC	0.68	0.28	1.74	0.84	1.64	1.29

Table 3. W-FULL minus W-CLIM ensemble mean differences of SST (in °C), surface heat fluxes (positive downward, in W m^{-2}) and total cloud cover (TCC) over the entire tropical Pacific (see Fig. 8e for basin boundaries), for the 1998–2012 (negative IPO) and 1979–1997 (positive IPO) periods. The 1979–2014 mean value for W-FULL is also given as a reference. Total HF designates the total heat flux. SW_{net} CS is the clear-sky surface shortwave flux.

	W-FULL minus W-CLIM		W-FULL
	1998-2012 (IPO-)	1979-1997 (IPO+)	1979-2014
SST (in °C)	-0.12	0.10	25.9
LW_{net} Surf (W m^{-2})	-0.12	0.37	-68.1
SW_{net} Surf (W m^{-2})	0.61	0.26	230.2
Sensible (W m^{-2})	-0.10	0.05	-17.2
Latent (W m^{-2})	0.75	-0.65	-130.0
Total HF (W m^{-2})	1.14	0.03	14.9
SW_{net} CS Surf (W m^{-2})	0.17	-0.12	283.5
TCC (%)	-0.38	-0.02	53.4

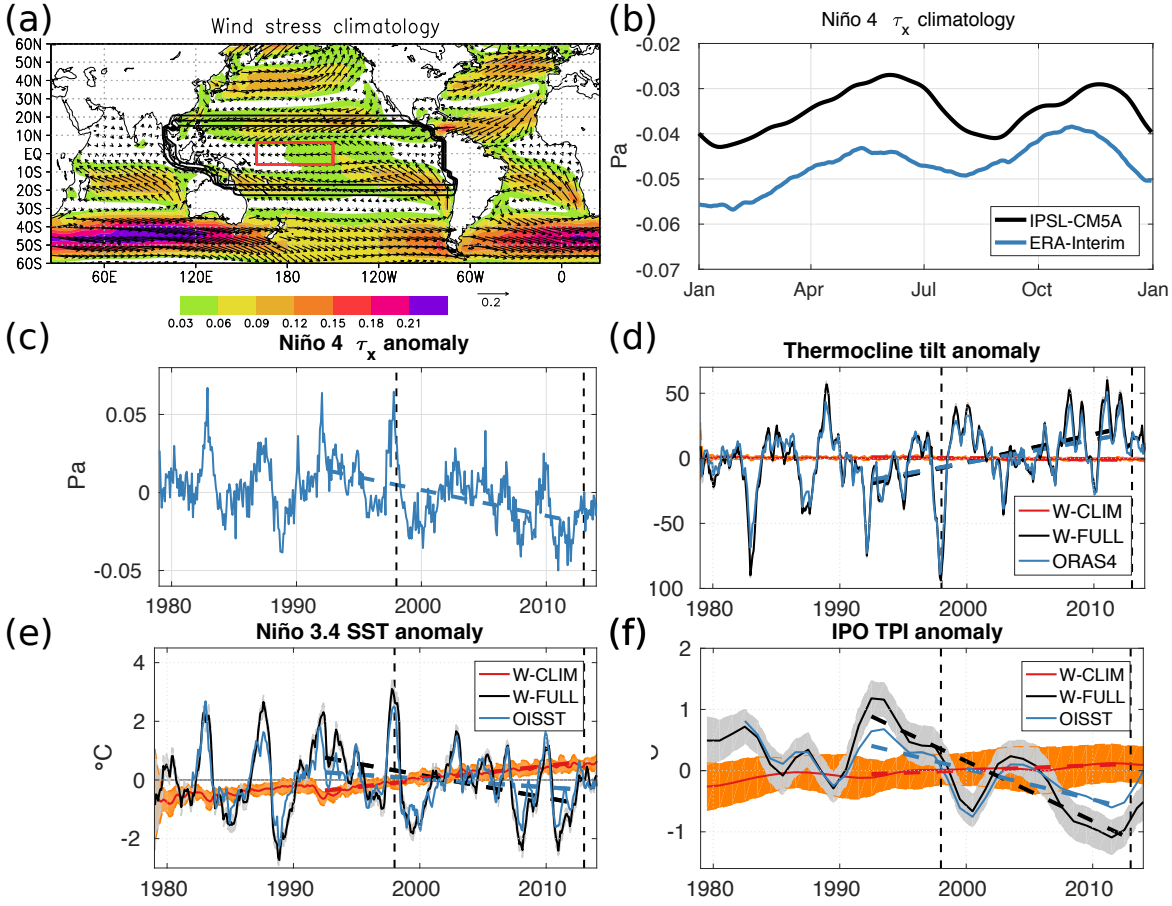

Figure 1: (a) Mean 1979–2014 IPSL-CM5A-LR surface wind stress climatology (vectors and shading), in Pa. Colors indicate the wind stress magnitude. The black contours (contour intervals 0.3, 0.6, and 0.9) delineate the mask used to prescribe the wind stress in the tropical Pacific. The red box indicates the Niño 4 region. **(b)** Wind stress climatology over Niño 4, in Pa, in IPSL-CM5A-LR historical (black) and ERA-Interim (blue). **(c)** Monthly Niño 4 wind stress anomalies from ERA-Interim applied in the W-FULL experiment, in Pa. **(d)** Monthly Pacific west–east thermocline (20°C isotherm depth) tilt anomalies. **(e)** Monthly Niño 3.4 SST anomalies. **(f)** IPO low-pass filtered SST tripole index (TPI) anomaly. Thick solid lines in (d–f) indicate ensemble means (black for W-FULL, red for W-CLIM) and observations (blue). Shading in (d–f) illustrates the ensemble spread, with the 95% confidence intervals. The dashed lines in (c–f) show the 1992–2012 annual mean trends, colored respectively as the data and simulations. The vertical dashed lines mark 1 January 1998 and 1 January 2013 (i.e. the negative IPO period).

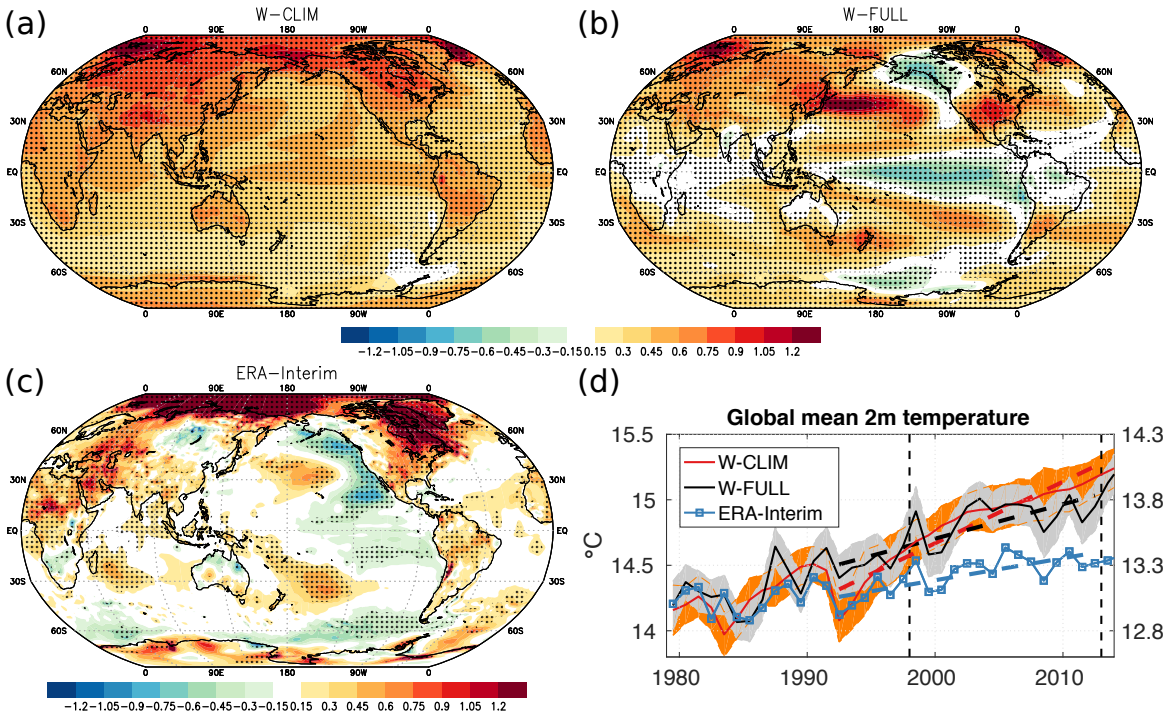

Figure 2. 1992-2012 2m temperature trend, in °C per decade for **(a)** W-CLIM, **(b)** W-FULL, and **(c)** ERA-Interim. Stippling denotes regions where the trends are significant at the 95% confidence level. **(d)** Globally-averaged annual mean 2m temperature, in °C, for W-CLIM (red), W-FULL (black), and ERA-Interim (blue); note that the simulations are offset by 1.2°C to correct for the mean temperature bias (right axis). Thick solid lines indicate the ensemble means; shading illustrates the ensemble spread, with the 95% confidence intervals. Dashed lines show the 1992–2012 linear trends. The vertical dashed lines mark 1 January 1998 and 1 January 2013.

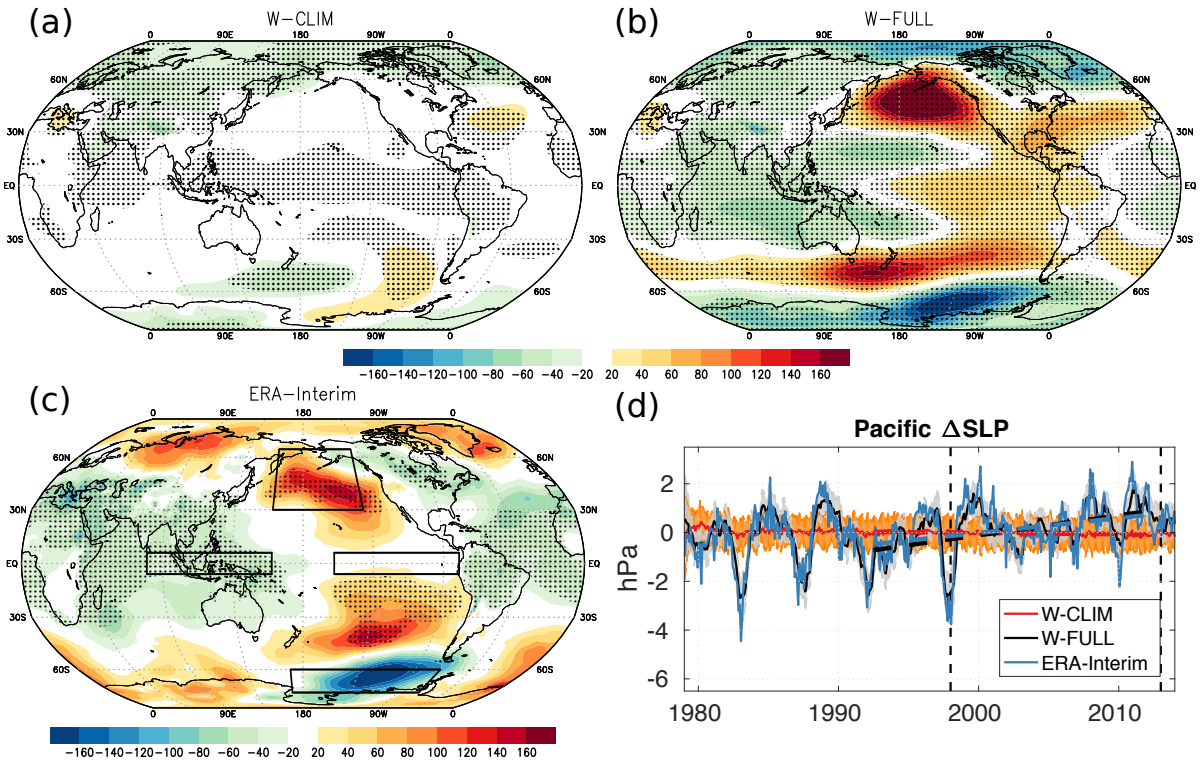

Figure 3. 1992–2012 annual mean SLP trends, in Pa per decade for **(a)** W-CLIM, **(b)** W-FULL, and **(c)** ERA-Interim. Stippling denotes regions that are significant at the 95% confidence level. Boxes in (c) delineate the regions used to compute the average SLP in the western and eastern equatorial Pacific (used in ΔSLP), North Pacific, and Amundsen Sea in Table 1. **(d)** Monthly Pacific ΔSLP anomalies, in hPa. Thick solid lines in (d) indicate the ensemble means; shading illustrates the ensemble spread, with the 95% confidence intervals; dashed lines show the 1992–2012 trends. The vertical dashed lines mark 1 January 1998 and 1 January 2013.

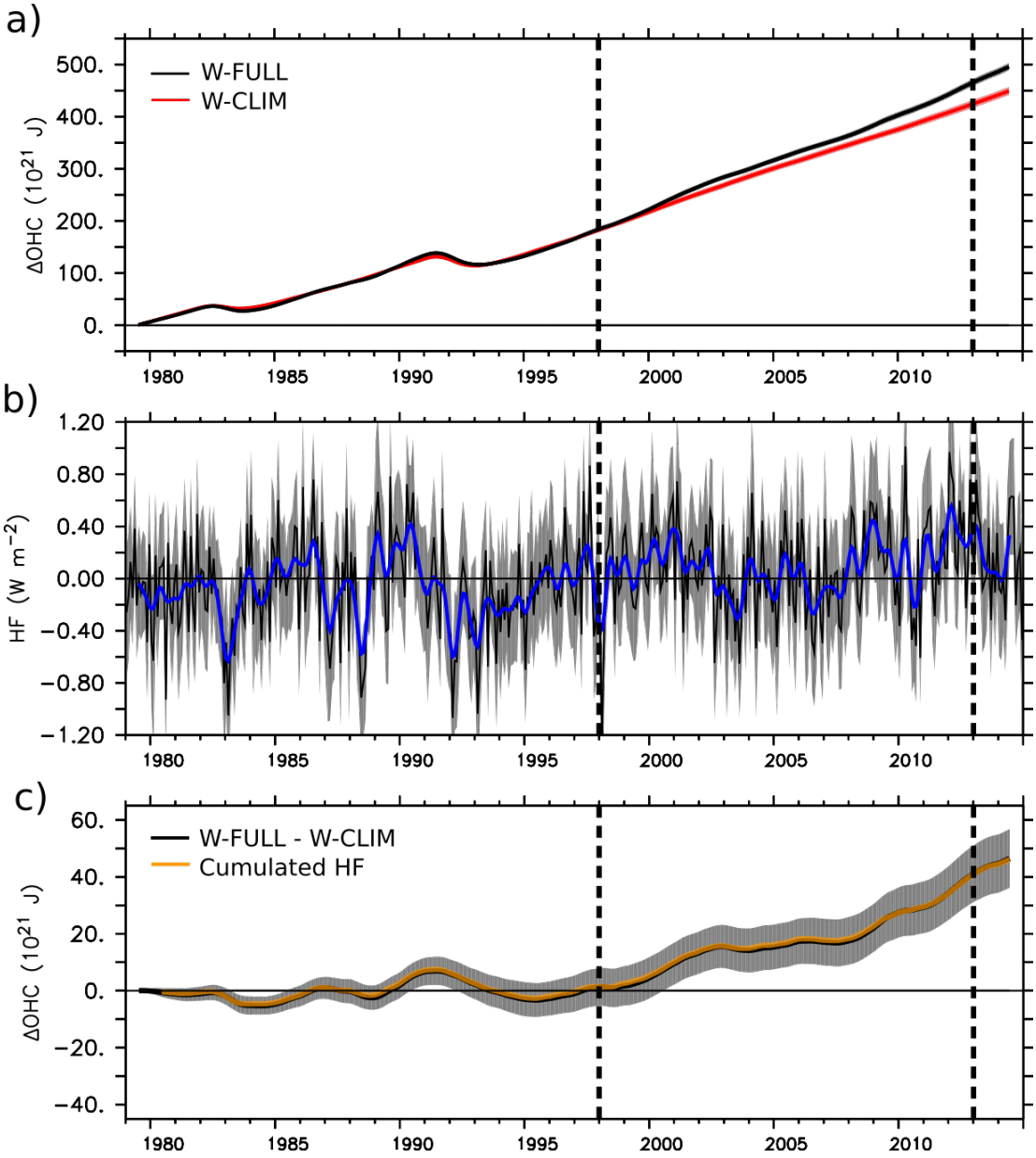

Figure 4. (a) Global W-FULL (black) and W-CLIM (red) ensemble mean OHC, in 10^{21}J. **(b)** Globally-averaged W-FULL minus W-CLIM ensemble mean deseasonalized monthly surface heat flux into the ocean, in W m^{-2} (positive downward). The thin black line represents monthly values, while the thick blue line is smoothed using a 12-month running mean. **(c)** Global W-FULL minus W-CLIM ensemble mean OHC (black), and the time-integrated net surface heat flux since 1 January 1979 (orange), in 10^{21}J. In (a) and (c) the time series are smoothed using a 12-month running mean. The shading in (b) and (c) indicates the 95% confidence intervals. The vertical dashed lines mark 1 January 1998 and 1 January 2013.

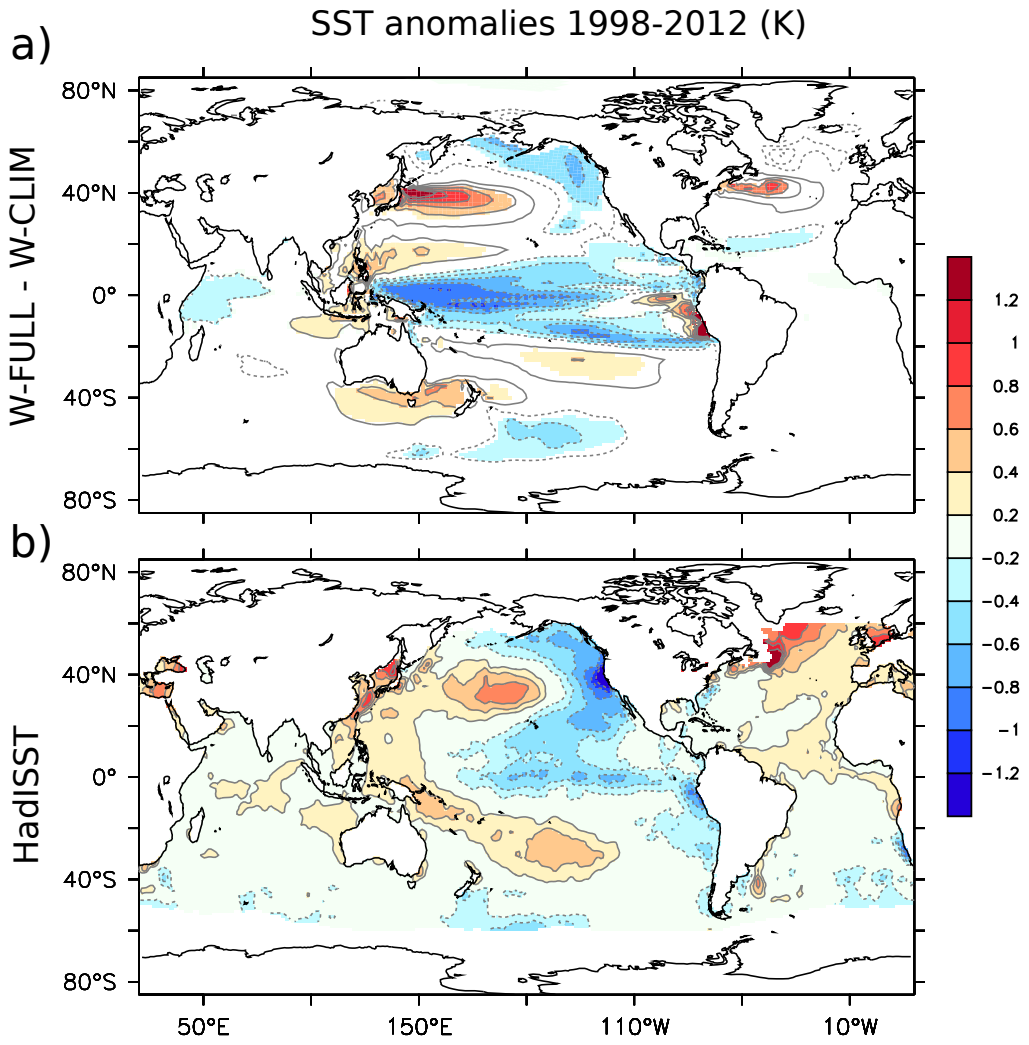

Figure 5. 1998–2012 average SST anomalies (in °C), from: **(a)** W-FULL minus W-CLIM; with shading indicating regions statistically significant at the 95% confidence level; **(b)** HadISST observations after removal of the global warming signal using an optimal linear inverse modeling filter.

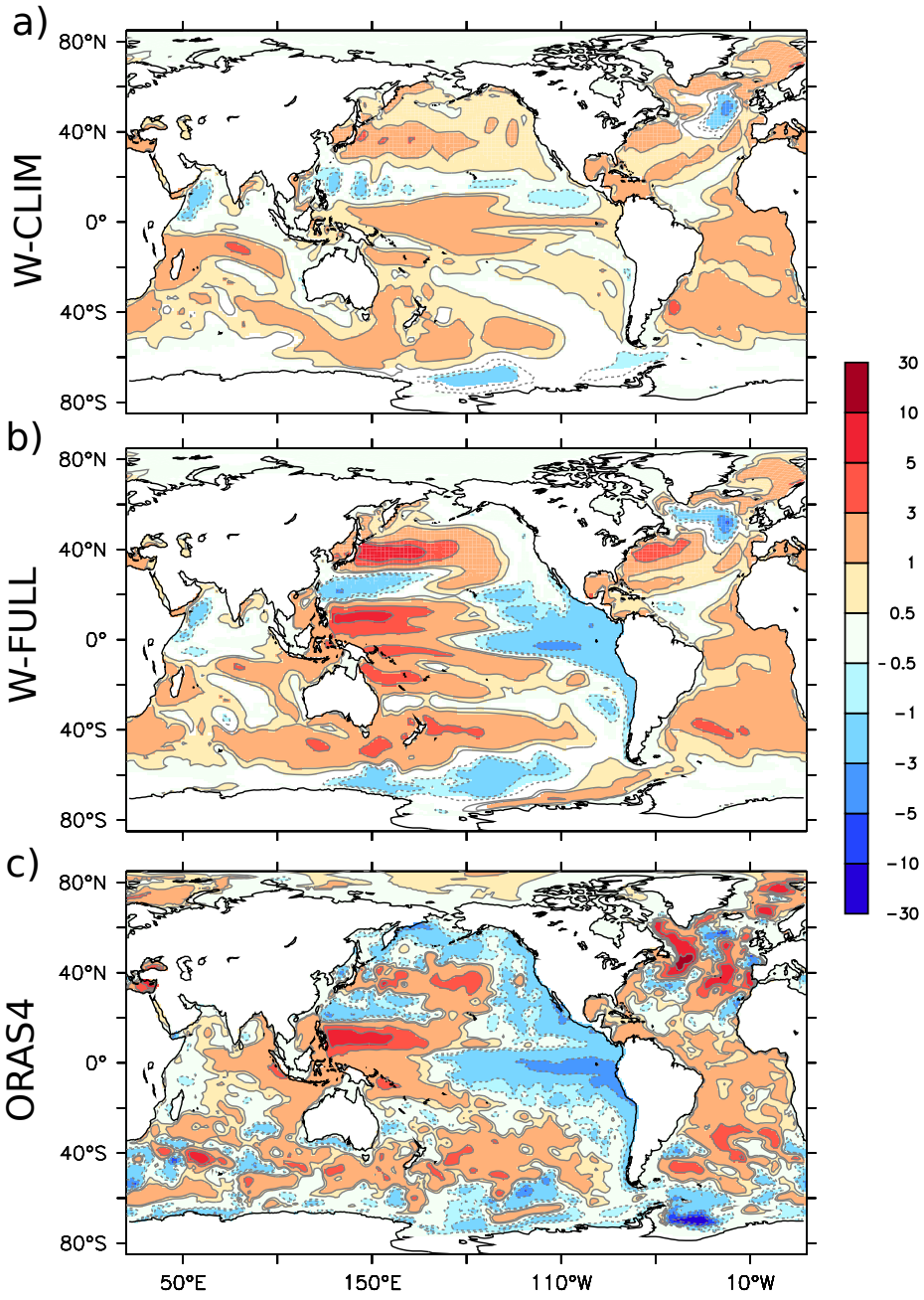

Figure 6. OHC change over the 1998-2012 period, ΔOHC, shown here in 10^9 J m^{-2} for the entire ocean column, in **(a)** W-CLIM, **(b)** W-FULL and **(c)** ORAS4.

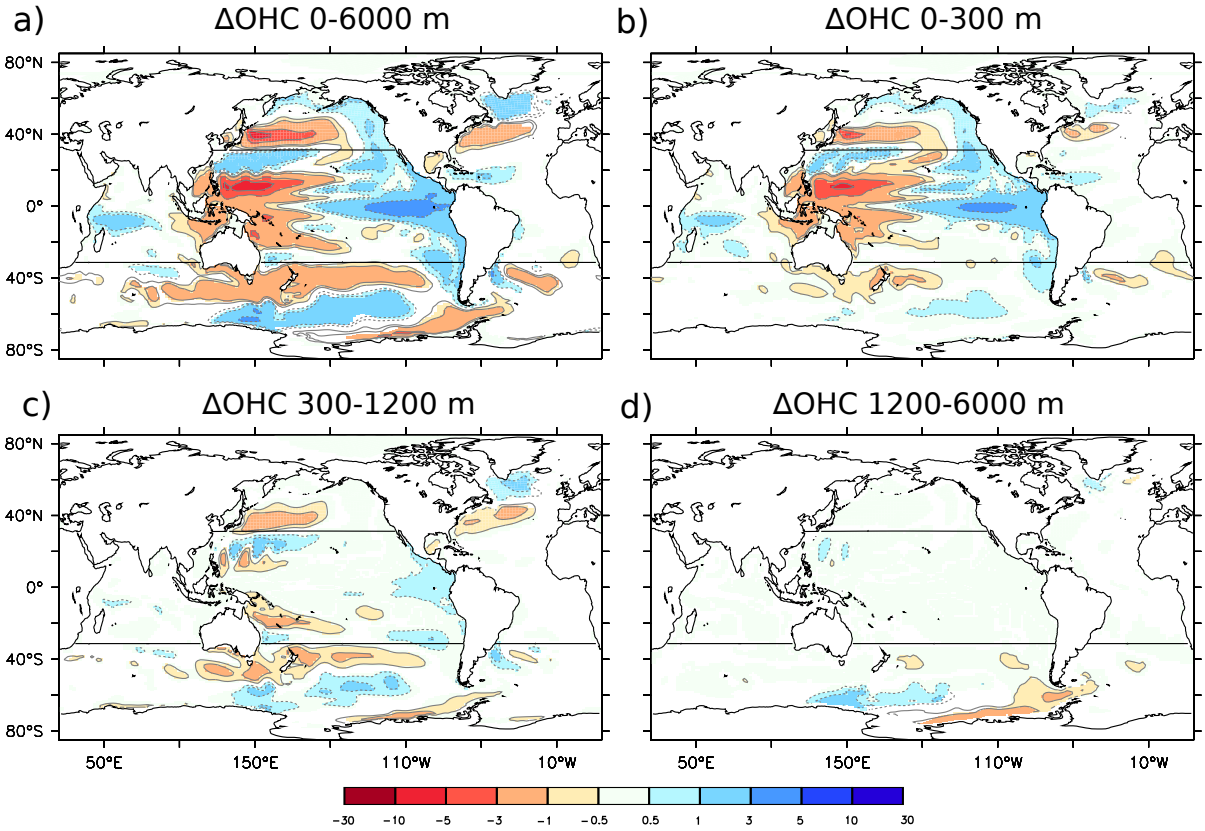

Figure 7. Vertical distribution of the W-FULL minus W-CLIM OHC change over the 1998-2012 period, ΔOHC_{-IPO}, in 10^9 J m^{-2}: **(a)** entire ocean column, **(b)** 0-300m, **(c)** 300-1200m, and **(d)** 1200m-6000m. The colors are plotted where significant above the 95% confidence level. The boundaries of the different basins used in Fig. 8 are indicated by black lines.

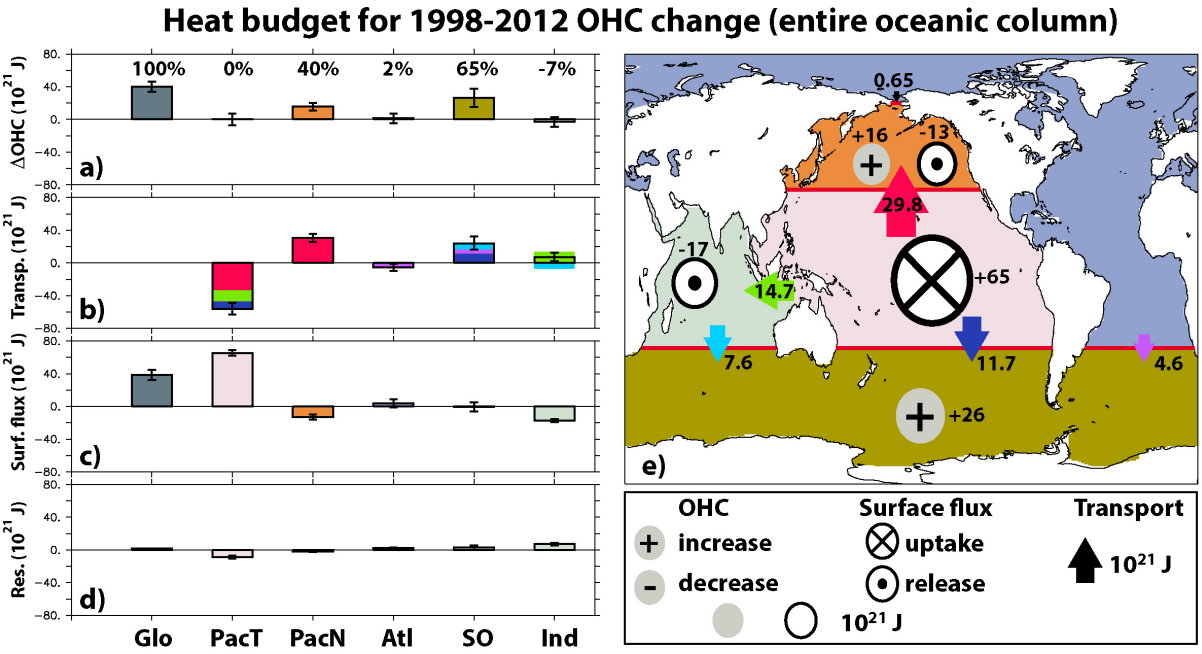

Figure 8. Regionally-integrated heat budget for the W-FULL minus W-CLIM OHC change over the 1998-2012 period (ΔOHC_{-IPO}): **(a)** ΔOHC_{-IPO} partitioned into the contributions from **(b)** ocean heat transport, **(c)** surface heat fluxes, and **(d)** the residual (see section 2.3 and Eq. (2) for more details). Glo, PacT, PacN, Atl, SO, and Ind respectively denote the global, tropical Pacific, North Pacific, Atlantic, Southern, and Indian Ocean domains, shown with distinct colors on panel (e). The percentages on panel (a) indicate regional contributions to the global OHC change. The colors on panels a, c, and d match those of the corresponding ocean basins on (e). The colors on panel b match those of arrows representing the transport between basins on panel (e). Error bars on panels a–d indicate the 95% confidence intervals. **(e)** Schematic summarizing the heat redistribution during 1998-2012. The grey circles represent OHC changes, white circles surface heat uptake, and arrows exchanges of heat between the basins (value indicated next to each symbol, in 10^{21} J). The area of the circles and arrows is proportional to the heat quantity, with scales given below panel (e).

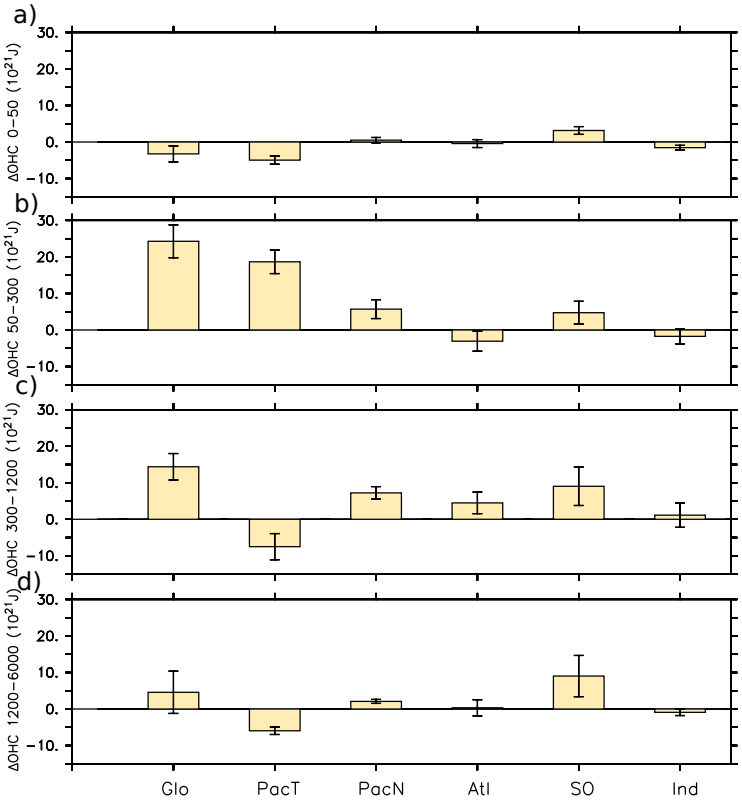

Figure 9. Regionally-integrated heat budget for the W-FULL minus W-CLIM OHC change over the 1998-2012 period (ΔOHC_{-IPO}) partitioned by depth: **(a)** 0-50m, **(b)** 50-300m, **(c)** 300-1200m, **(d)** 1200-6000m. Glo, PacT, PacN, Atl, SO, and Ind respectively denote the global, tropical Pacific, North Pacific, Atlantic, Southern, and Indian Ocean domains, shown with distinct colors in Fig. 8e. Error bars indicate the 95% confidence intervals.

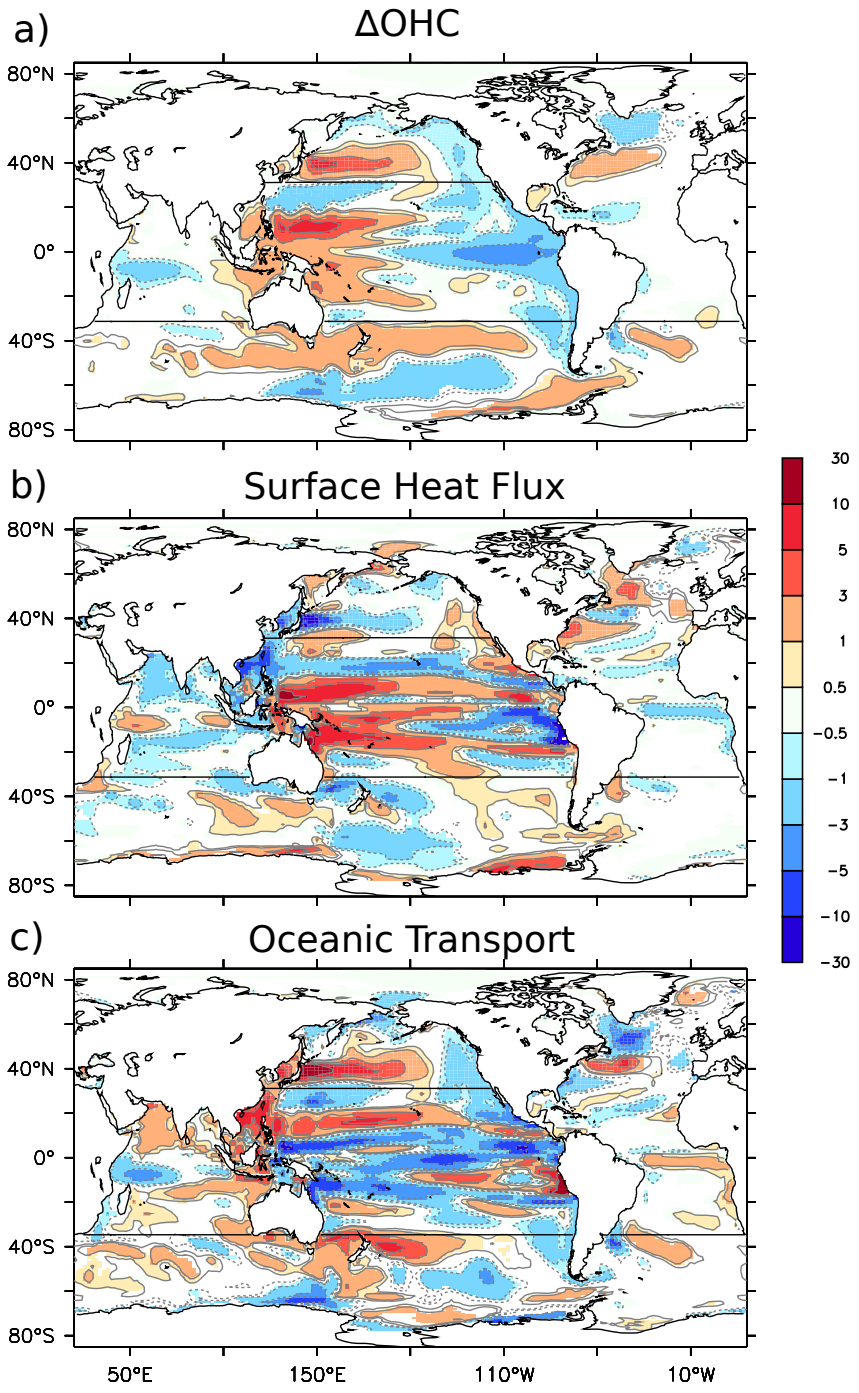

Figure 10. (a) W-FULL minus W-CLIM OHC change over the 1998-2012 period, ΔOHC_{-IPO}, in 10^9 J m^{-2}, and contributions from **(b)** surface heat fluxes and **(c)** oceanic transport. The colors are plotted only where significant above the 95% confidence level.

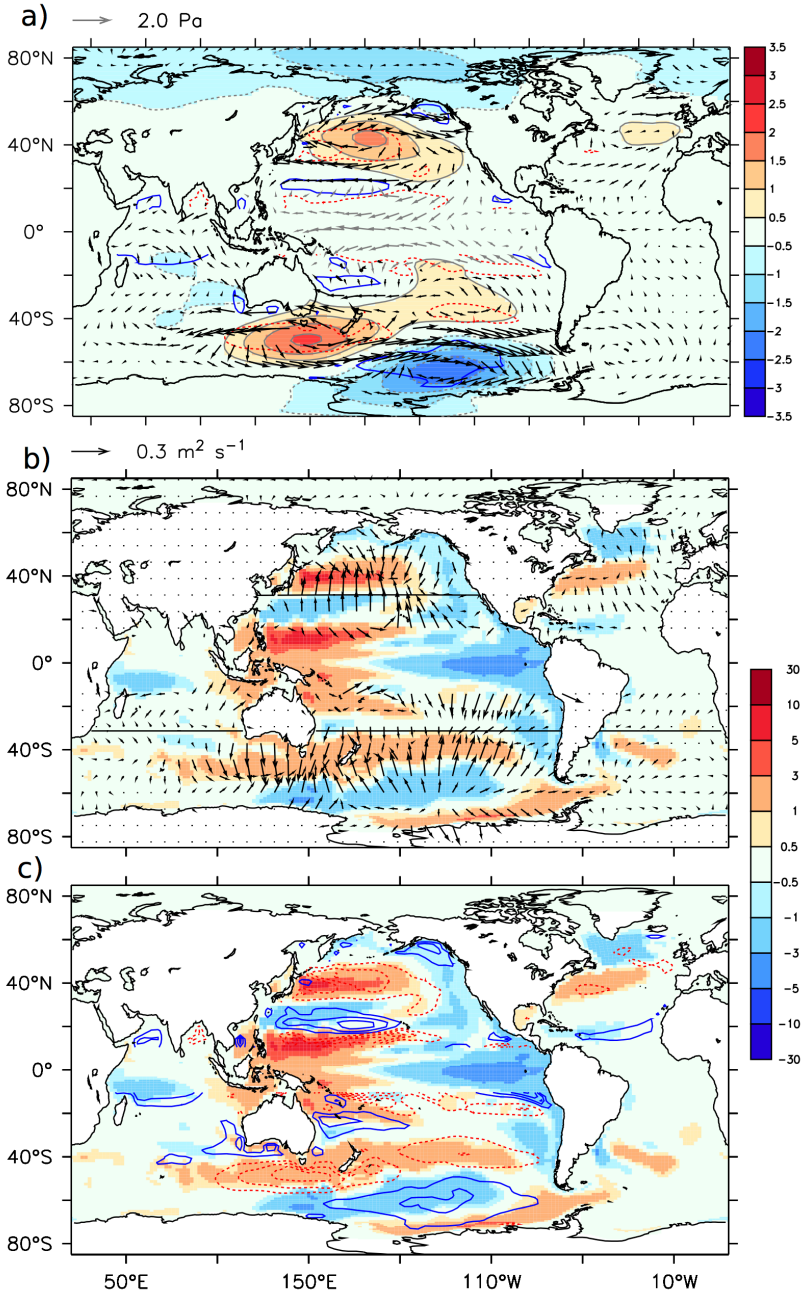

Fig. 11. (a) W-FULL minus W-CLIM 1998–2012 average SLP (hPa, shading); Ekman pumping (blue contours for positive and red contours for negative values; contour interval 1.5 10^{-7} m s^{-1}); and wind stress (Pa, vectors). Wind stress vectors are grey inside the tropical Pacific (i.e. the region where the observed wind stress anomaly is prescribed in W-FULL), and black outside it. **(b)** W-FULL minus W-CLIM 1998–2012 change in ocean heat content, ΔOHC_{-IPO} (10^9 J m^{-2}, shading) and Ekman transport (arrows). **(c)** Same as (b), with the 1998-2012 average Ekman pumping (blue contours for positive and red contours for negative values; contour interval 10^{-7} m s^{-1}).

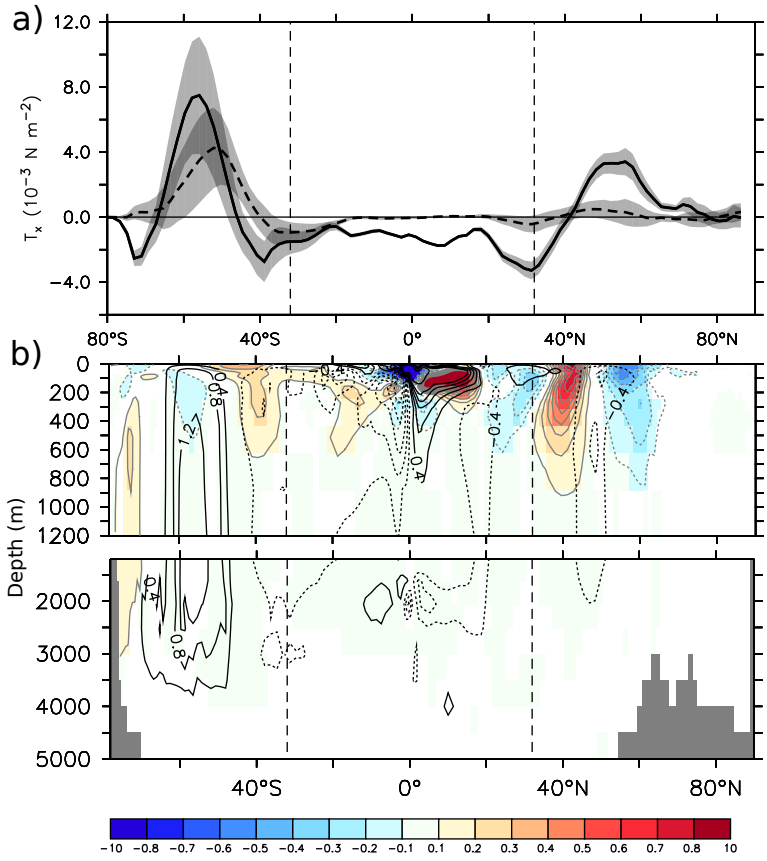

Figure 12. Zonal-mean W-FULL minus W-CLIM: **(a)** 1998-2012 zonal wind stress (black, in 10^{-3} Pa). The black dashed line indicates the 1998-2012 anomalous zonal wind stress (relative to 1979-2014) in W-CLIM (10^{-3} Pa). Shading indicates the 95% confidence intervals. **(b)** Global zonal-mean potential temperature change over 1998-2012 (°C, shading) and anomalous zonal-mean residual streamfunction (Sv, contours). Note the different vertical scales for the top 1200 m and below. In (b), colors are plotted only where significant above the 95% confidence level.

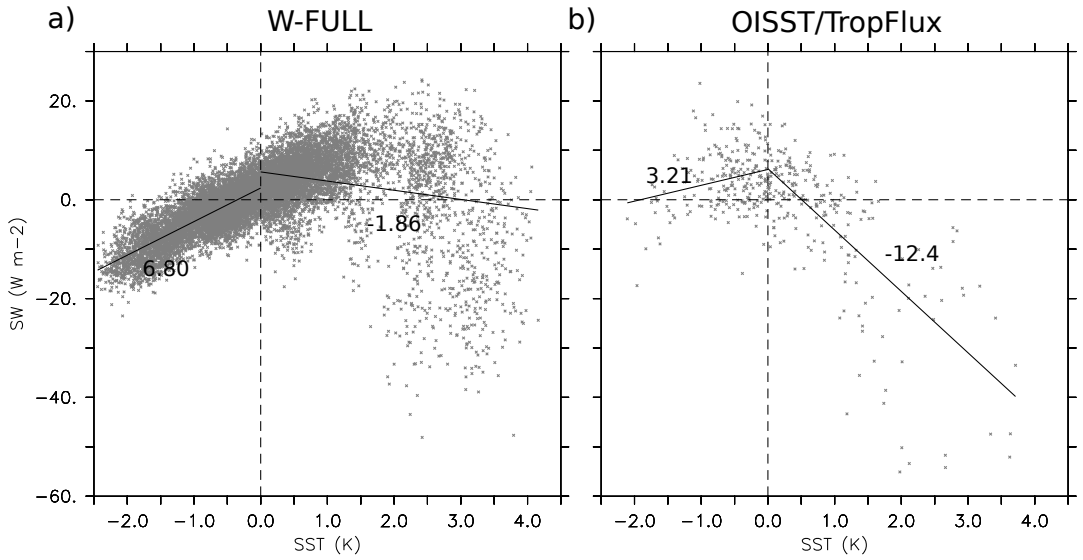

Figure 13. Scatter plot of average Niño 3 region (150°W-90°W, 5°S-5°N) surface net shortwave radiation (positive downward, in W m^{-2}) versus SST (in °C) monthly anomalies in **(a)** the W-FULL simulation, and **(b)** observations (TropFlux and OISST). The lines indicate the regression slopes of surface shortwave radiation onto SST, computed separately for positive and negative SST anomalies. The values of the slopes (in W m^{-2} K^{-1}) are also indicated.

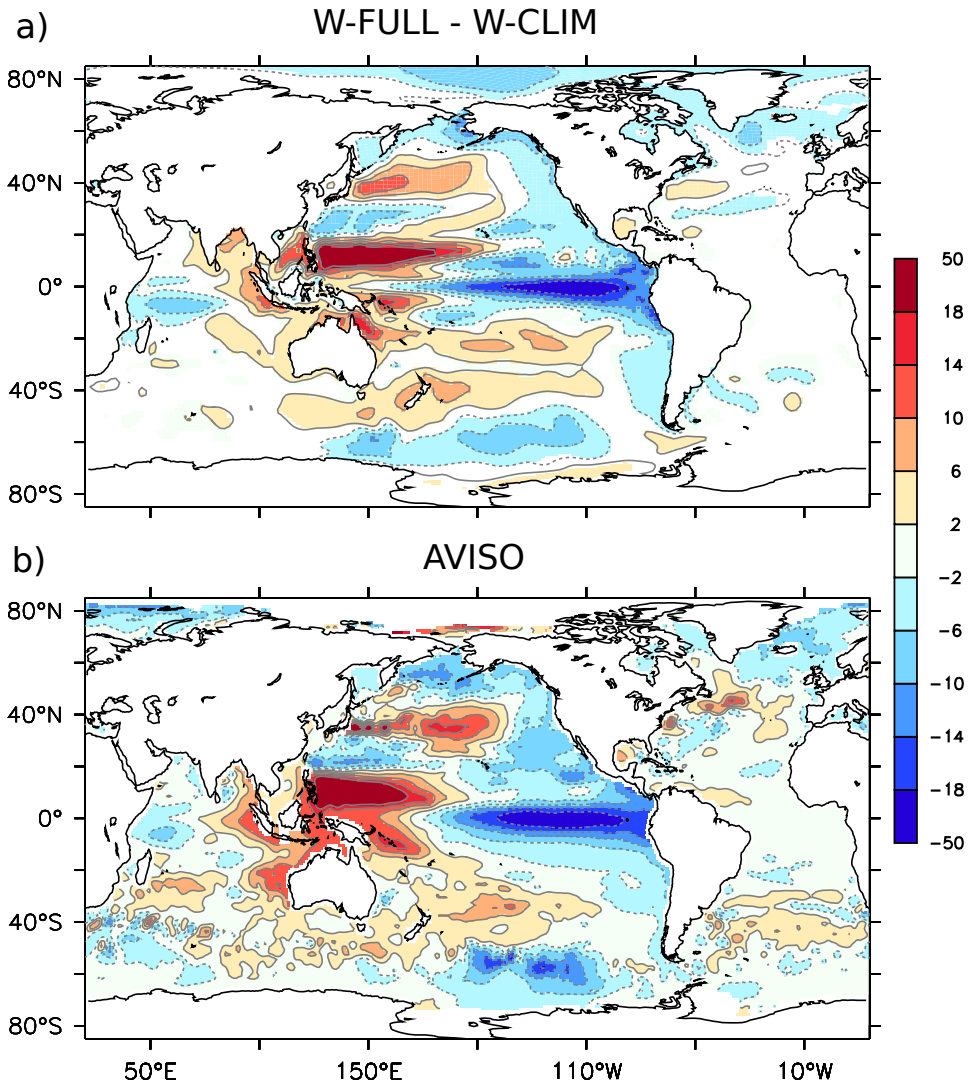

Figure 14. Sea surface height change from 1998 to 2012 (in cm) for **(a)** W-FULL minus W-CLIM; **(b)** AVISO observations. In (a) and (b), we remove the global mean sea surface height increase: this removes the cryosphere-related and land storage, but also the globally-averaged thermosteric effect that is not reproduced by the model (Greatbatch, 1994).

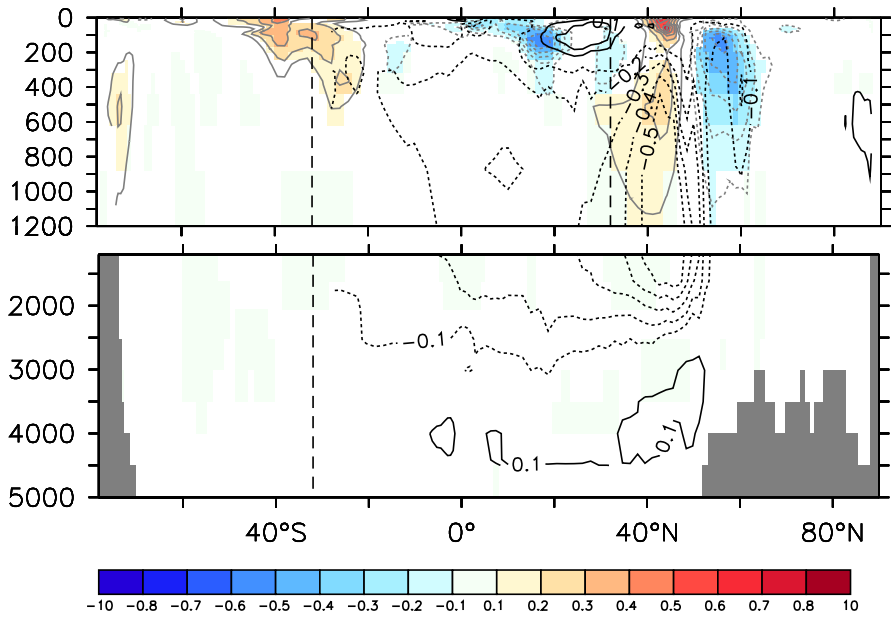

Figure 15. Atlantic zonal-mean potential temperature change from 1998 to 2012 (in °C, shading), and 1998–2012 average anomalous residual zonal-mean streamfunction (Sv, contours) for W-FULL minus W-CLIM. The colors are plotted only where significant above the 95% confidence level. Note the different vertical scales for the top 1200 m and below.